Sensor Technologies for Nuclear Physics Applications

A Thesis Presented for the

Master of Science

Degree

The University of Tennessee, Knoxville

Corey Edward Gilbert

August 2019

© by Corey Edward Gilbert, 2019
All Rights Reserved.

I dedicate this thesis to Lady Arwen.

Acknowledgments

I would like to thank my parents and grandparents for their unending support and motivation during my time in college.

I also would like to thank Alfredo for providing me with the opportunities to perform this work and helping me transition into the professional world.

Thank you to Jorge, David, Geoff, and all the HFIR staff for helping me learn about HFIR and the experimental methods used during this project.

Thank you to my colleagues, Elisa and Jeremy for helping me throughout my projects and guiding me when I get stuck.

Last but not least, thank you to all the administrative support in both ORNL and UTK.

Abstract

This work describes the development of environmental monitoring systems based on low-cost electronics and mini-computers (Raspberry Pi), for two projects in nuclear physics. The first project is the PROSPECT liquid scintillator based antineutrino experiment. The second project refers to a deployment of gamma-ray detection systems underwater to obtain a nondestructive nuclear fuel element assay. Both of these projects are based in the High Flux Isotope Reactor (HFIR) in Oak Ridge National Laboratory (ORNL) with different objectives. We describe the scientific goals of each project.

PROSPECT's primary goals are to probe short-baseline oscillations and perform a precise measurement of the U-235 reactor antineutrino spectrum using an array of optical cells to guide scintillation light to photomultiplier tubes (PMTs). The PMTs inside PROSPECT can be exposed to stray magnetic fields from strong superconducting magnets operating on the experiment hall one floor below the detector. High magnetic fields can directly influence the PMT gain and pulse shape; this motivated us to deploy a system of magnetometers around the detector to monitor stray background magnetic fields.

The underwater gamma-ray detection system is primarily focused on measuring the gamma spectrum from fuel elements to analyze position-dependent isotopic composition. To protect the gamma-ray detection equipment from water damage, an essential component of this system is a hygrometer developed for determining if the underwater housing has been compromised.

Both Raspberry Pi based monitoring systems were designed, tested and built, based on the needs of the specific experiment. The Raspberry Pi is the third best selling computer brand in the world and is based on a single board processor chip. These computers are light, low-cost, portable and adaptable for a variety of applications. Initially designed for

the vast learning opportunities for educational programs in computer science, Raspberry Pi's have found purpose in many other scientific fields. In this work, we use the Raspberry Pi as a micro-controller, data acquisition system and a server for live graphical representation. The systems have been fully developed and successfully implemented into each experiment, providing real-time environmental parameter monitoring.

Table of Contents

1 Introduction **1**

1.1 Motivation 1

1.2 Thesis Outline 2

2 PROSPECT **4**

2.1 Motivation 4

2.1.1 Historical Considerations of Antineutrinos 4

2.1.2 Antineutrinos from Reactors 4

2.1.3 High Flux Isotope Reactor 5

2.2 Detector Design 8

2.2.1 Method of Detection for Antineutrinos 11

2.3 Background Environments in Neutrino Physics 11

3 Magnetometer System **15**

3.1 Introduction 15

3.2 Magnetic Backgrounds 16

3.2.1 Magnetic Field Effects on Photo Multiplier Tubes 17

3.2.2 Magnetic Shielding 17

3.3 Design of a Magnetometer System 20

3.3.1 Raspberry Pi 20

3.3.2 I^2C Introduction 20

3.3.3 Magnetometer Chip 21

3.3.4 Multiplexer 22

3.3.5 I2C Signal Extenders . . . 22
3.4 Magnetometer System Setup . . . 23
3.4.1 Slow Control Communication Protocol . . . 23
3.4.2 Deployment Around PROSPECT . . . 24
3.5 Calibration . . . 24
3.5.1 Lakeshore Hall Probe . . . 24
3.5.2 Metrolab Hall Probe . . . 26
3.5.3 Calibration Program . . . 27
3.6 Measurements . . . 29
3.6.1 Mapping Around the Detector . . . 29
3.6.2 Bench Tests for Stability and Calibration . . . 29
3.6.3 Measurements Around PROSPECT . . . 29
3.7 Conclusions with Magnetometers . . . 31

4 Gamma Scanning Project **33**
4.1 Introduction . . . 33
4.1.1 Detector Housing . . . 33
4.2 Detector Testing Station . . . 34
4.3 Choice of Gamma Ray Detection Technology . . . 36
4.4 Semiconductor Detectors . . . 37
4.4.1 Semiconductor Gamma Ray Detection Mechanism . . . 37
4.5 Cadmium Zinc Telluride Detector . . . 38
4.5.1 Applications in Other Areas of Physics . . . 39
4.6 Detector Housing Hardware Upgrade . . . 41
4.6.1 Hygrometer Chip . . . 41
4.6.2 Data Collection . . . 43
4.6.3 InfluxDB . . . 43
4.6.4 Docker . . . 43
4.6.5 Grafana Server . . . 44
4.6.6 Humidity Monitoring Setup and Configuration . . . 44

4.7 Hygrometer Results . . . 45
4.7.1 Testing Setup . . . 45
4.7.2 Sealed Bucket Tests . . . 45
4.7.3 Results Inside Empty Detector Housing . . . 47
4.8 Gamma Scanning in Reactor Pool . . . 47
4.9 Conclusion . . . 49

5 Conclusions and Future Work **51**
5.1 Summary of Results . . . 51
5.2 Future Work . . . 52

Bibliography **53**

Vita **59**

List of Tables

4.1 Comparison between different semi-conductor and scintillator based detectors. 37

4.2 Average rate of change of the humidity for 1 minute after leak is injected into the sealed bucket. The initial conditions for temperature and humidity are given. 46

List of Figures

2.1 Antineutrino spectrum showing a local excess in the 5 MeV region [1]. 6

2.2 Reactor Antineutrino flux deficit compared to expected theoretical prediction [1]. 6

2.3 PROSPECT's location relative to the HFIR Core. 6

2.4 Fuel plate arrangement in HFIR core. 7

2.5 Comparison of different research and commercial reactor cores. The HFIR core is about half the diameter of ILL and operates with about 1.4 times more power. 7

2.6 Expected $\bar{\nu}_e$ spectrum. 9

2.7 Expected $\bar{\nu}_e$ from ^{235}U and ^{239}Pu. 9

2.8 Fission fragments of ^{235}U. 10

2.9 Inverse Beta Decay Process. 12

2.10 Cross-sectional view of PROSPECT showing segmented active detector and shielding placements. 12

2.11 Simulated signal and background spectra. Background is primarily from cosmogenic fast neutrons. Cuts are applied based on IBD timing and spacial characteristics. Adapted from [2]. 14

3.1 Experiment hall at HFIR. 16

3.2 Relative output of PROSPECT PMT with varying magnetic flux 18

3.3 Relative gain of Hamamatsu PMT with varying magnetic flux densities . . . 18

3.4 Schedule of magnet operation on each beamline during the operation of PROSPECT. 18

3.5 ET 9372B PMT. 19
3.6 PMT cell setup inside The PROSPECT Detector. 19
3.7 Basic transmission of request and response over I^2C communication protocol. 22
3.8 Screenshot of the slow control server live plots. 23
3.9 Position of the sensors attached to the detector. 25
3.10 Photo of Magnetometer attached to PROSPECT. 25
3.11 Z scan of the magnetic field from magnetized chassis using the Lakeshore single-axis hall probe. 26
3.12 Photo of the lid with a magnetometer attached. 26
3.13 Lakeshore hall probe and zero gauss chamber for calibration. 27
3.14 Metrolab hall probe in custom 3D printed stand for calibration. 27
3.15 x- and y-axis magnetic field plotted before axes shift calibration. 28
3.16 x- and y-axis magnetic field plotted after axes shift calibration. 28
3.17 Angled view of PROSPECT detector with magnetic field vectors plotted around the edge. 30
3.18 Top view of the detector with magnetic field magnitude plotted as a heat map along the edges. 30
3.19 Magnetic field measured by 6 sensors before and after calibration in a static magnetic background. 30
3.20 Overnight stability of magnetometers after calibration. 30
3.21 Each sensor around PROSPECT reacting to the testing of Mag-E on HB-2A. 32

4.1 Underwater gamma-ray detector housing [3]. 34
4.2 Corey, Dr. A Galindo-Uribarri and the 1500 gallon bucket. 36
4.3 View of the housing submerged in the bucket. 36
4.4 Energy band structure for conductors, semiconductors and insulators. 38
4.5 Calibration spectrum of CZT detector using a variety of sources. 40
4.6 Calibration curve of CZT detector using a variety of sources. 40
4.7 View of the back of the RPi 7 inch touchscreen to show mounting of I2C signal extender and RPi. 42

4.8 Locally hosted Grafana server to display the environmental conditions inside the housing. 42
4.9 Setup of 5 gallon o-ring sealed Leaktite bucket. 46
4.10 View of the testing bucket with attached electronics. 46
4.11 Lowering of submarine into the testing bucket while watching the leak detection system server for alerts. 48
4.12 housing being submerged with a faulty o-ring seal. 48
4.13 Submerged housing over 60 hours with no sign of leak. 48
4.14 Underwater Source check with 4ft. tube and double collimation setup. Fitting is done in Radware where we extract peak parameters (ie. width) and check energy calibration. 49

Chapter 1

Introduction

This work focuses on the development and characterization of compact, low cost environmental monitoring systems implemented in nuclear physics experiments. The monitoring system provides real-time notification of the surrounding environmental parameters and features a user programmable alarm that can be configured to send a message via email if an alarm condition occurs. This compact but powerful monitoring system is adaptable to the specific needs of an experiment and can host up to 1008 sensors of any variety.

1.1 Motivation

One of the most exciting fields in physics is the investigation of the properties of neutrinos. This particle has captivated the imagination of scientists and currently is the focus of attention for large research collaborations and projects. Accelerator and reactor based projects have been launched to study this fascinating particle. Research efforts have led to unexplained deficits in total flux measurements that might hint at the existence of a new type of neutrino, as well as unexpected spectral distortions, section 2.1.2. These open questions will hopefully be answered by the Precision Reactor Oscillation and Spectrum Experiment (PROSPECT) measuring the antinuetrinos emitted from the highly enriched uranium (HEU) research reactor core at the High Flux Isotope Reactor (HFIR).

The operation of HFIR is important to a large community of neutron scatterers, isotope production, and PROSPECT. HFIR, being a research reactor, has beam-lines for

neutron experiments that use strong magnets which can produce a magnetic background for PROSPECT. The first part of this work describes the implementation of a magnetic background monitoring system for PROSPECT.

In November of 2018, the HFIR reactor was shut down due to fuel element abnormalities. This shutdown opened up an opportunity to analyze the fuel element in search for defects using gamma-ray detection devices in an effort to speed up the recovery process. The challenging environment of a reactor pool necessitated a robust, well-shielded and watertight system to house the gamma-ray detectors.

To protect the gamma-ray detection equipment from water damage, an essential component of this system is a humidity monitoring system developed for determining if the underwater housing has been compromised. This humidity monitor is composed of a Raspberry Pi, as the data acquisition and server host, and a hygrometer chip situated inside of the detector housing.

Both systems were developed in a short amount of time, with a low cost compared to commercially available monitors and can easily be adapted to other experiments. The Raspberry Pi systems are very customizable to the unique applications and needs of the users within a lab environment without the need for additional infrastructure.

1.2 Thesis Outline

Chapter 2 introduces the PROSPECT experiment including detector layout, detection method, and description of the experiment location and source of neutrinos.

Chapter 3 describes the work done for the PROSPECT experiment to introduce a Raspberry Pi based monitoring system for the magnetic field backgrounds around the PROSPECT Detector. A description about the motivation behind this system and the effects that a strong magnetic field could have on the precise measurement of PROSPECT is given. This chapter goes into specific details about the sensors communication method with the Raspberry Pi, as well as with the PROSPECT slow control system for environmental parameter data logging.

Chapter 4 introduces the gamma scanning project for a nondestructive assay of nuclear fuel elements in a reactor pool using gamma ray detection technology contained in a water-tight detector housing. Specific details about the system and server design and communication to display the environmental parameters inside of the detector housing are discussed.

Chapter 2

PROSPECT

2.1 Motivation

2.1.1 Historical Considerations of Antineutrinos

The continuous spectrum of measured electrons from nuclear beta decay in the early 1900s hinted at the possibility of un-conserved energy in beta decay. In the 1930s, this anomaly led to the postulation of another light, charge-neutral particle the neutrino, later to be determined an electron antineutrino ($\bar{\nu}_e$), that carried the missing energy with it after the beta decay process [4]. The issue with this theorized particle is that the cross-section is so small and its interaction with matter is so weak that it was not measured until the 1950s in the Savannah River nuclear reactor. The Savannah River plant was able to provide flux of about $5\text{x}10^{13}$ neutrinos with 3 being detected each hour in the Cowan-Reines liquid scintillator based neutrino experiment. This was the start of reactor based, large volume detectors for neutrinos [5].

2.1.2 Antineutrinos from Reactors

Nuclear Reactors are able to provide an enormous flux of $\bar{\nu}_e$ in the process of beta decay, $\sim$6 per fission event. Using this excellent source of neutrinos, a recent series of discrepancies have been identified between total flux measured at nuclear reactors [6, 7, 8, 9, 10] and theoretical predictions [11].

Measurements of the antineutrino spectrum made at Daya Bay [1], Reno [12], and Double Chooz [13] show a spectrum that is inconsistent with the Huber-Mueller model [14] in the 5-9 MeV region (figure 2.1). The Huber-Mueller model combines the *ab initio* approach, where the $\bar{\nu}_e$ spectrum is calculated as a sum from all the fission products in ^{235}U, and the reference electron spectra measured at ILL reactor in Grenoble [15]. Daya Bay [1] also reports an overall flux deficit from the predicted flux of about 3% (figure 2.2). These measurements are interesting for studies on short-baseline antineutrino oscillations [16] in the m to km scale and have prompted some very interesting physics experiments. With PROSPECT only 7 m from a HEU reactor core, it is expected that these anomalies can be addressed.

The Precision Reactor Oscillation and Spectrum Experiment, PROSPECT, is designed to address the reactor neutrino flux anomaly [14, 15] by precisely measuring the antineutrino spectrum and searching for antineutrino oscillations with high resolution (4.5% energy resolution at 1 MeV) and short baseline measurements. PROSPECT is operating 7m$\pm$0.1 away from the compact research reactor core of the High Flux Isotope Reactor (HFIR) at Oak Ridge National Laboratory (ORNL), figure 2.3. In the next section, we briefly describe some relevant characteristics of HFIR.

2.1.3 High Flux Isotope Reactor

Operating at 85 megawatt (MW), the 93% highly-enriched uranium-235 (HEU) core of HFIR provides one of the highest steady-state neutron fluxes of any research reactor in the world [17]. HFIR operates with an approximate duty cycle of 42%, with $\sim$24 days of reactor on and followed by $\sim$35 days of reactor off maintenance period with fresh fuel installed, which thereby allows us to well characterize the background. HFIR has a very compact core (diameter: 43.5 cm, height: 50.8 cm) making it a "point-like" source of neutrinos [18]. Figures 2.4 & 2.5 show the HFIR fuel plate arrangement and a comparison of sizes between various reactor cores from a commercial power reactor core to other research reactor cores.

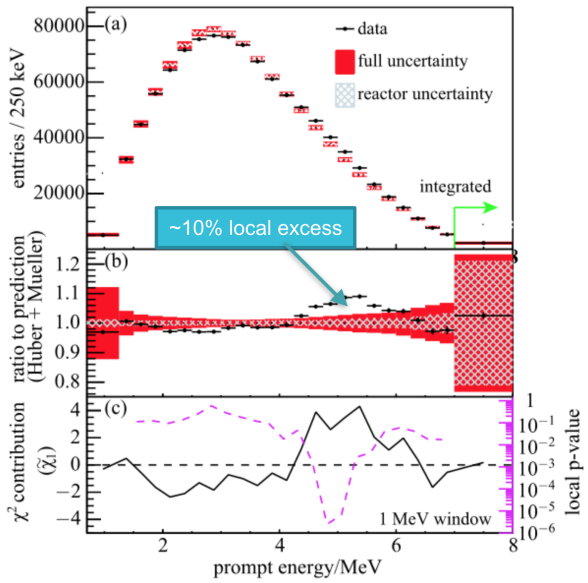


Fig. 2.1: Antineutrino spectrum showing a local excess in the 5 MeV region [1].

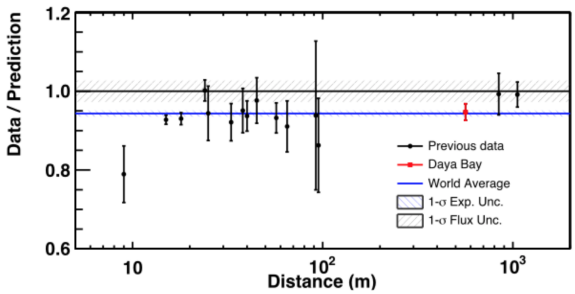


Fig. 2.2: Reactor Antineutrino flux deficit compared to expected theoretical prediction [1].

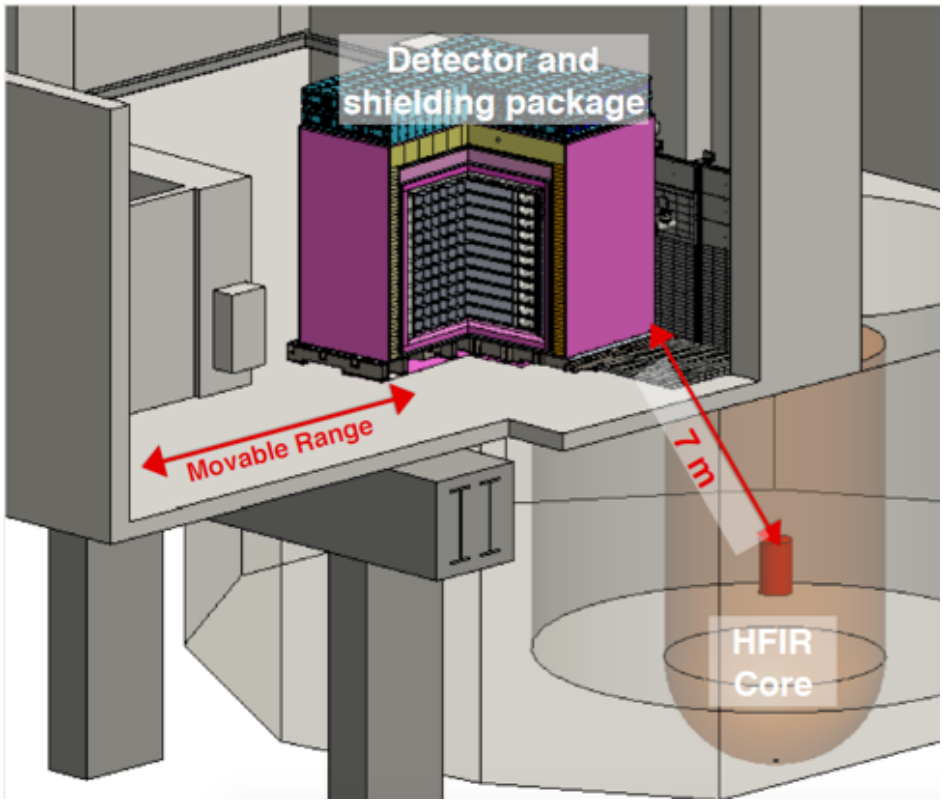


Fig. 2.3: PROSPECT's location relative to the HFIR Core.

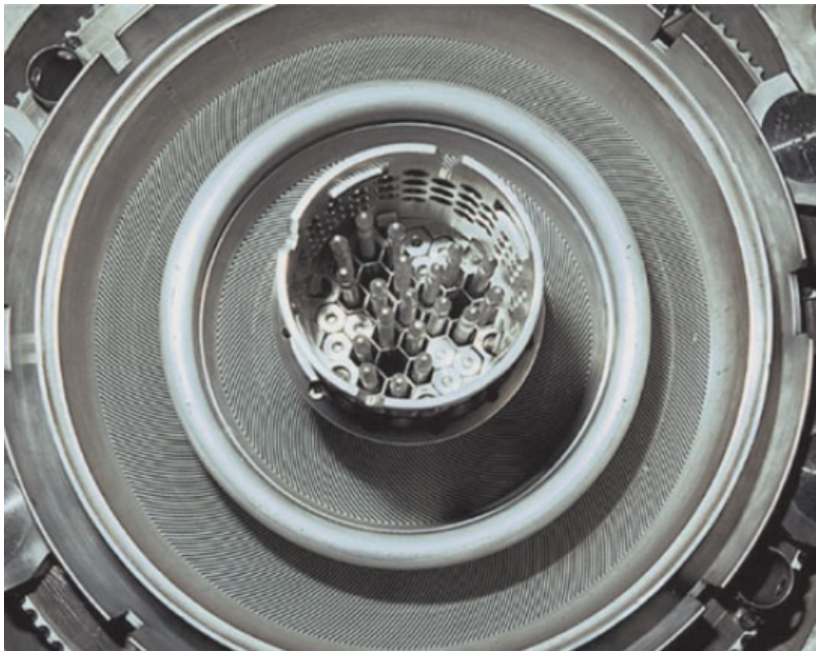


Fig. 2.4: Fuel plate arrangement in HFIR core.

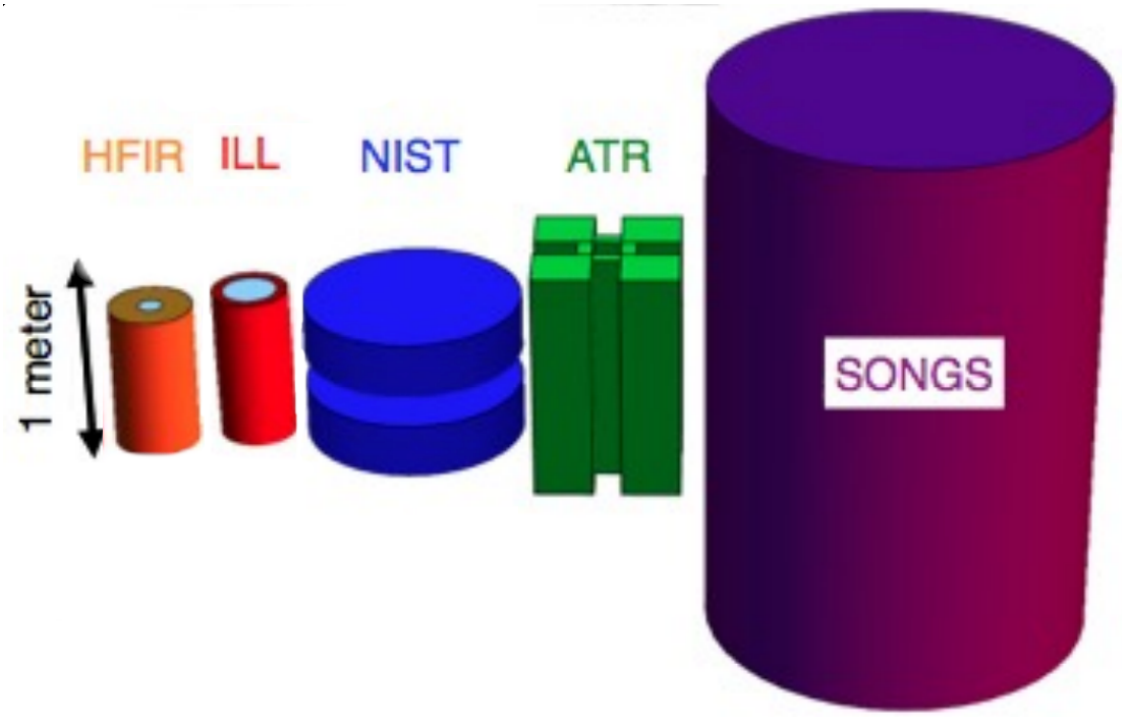


Fig. 2.5: Comparison of different research and commercial reactor cores. The HFIR core is about half the diameter of ILL and operates with about 1.4 times more power.

HFIR is a research reactor that provides a large flux of neutrons for the neutron scattering community. This reactor is well characterized, well understood, and quality reactor power models have been developed. As local research group at ORNL we have easy access to the reactor experiment hall, as well as to the area where PROSPECT is located. One other advantage is the use of 93% HEU fuel. The Reduced Enrichment for Research and Test Reactors (RERTR) Program [19] focuses to minimize the use of HEU in civil nuclear applications. HFIR is still operating with HEU and official plans for changing have not been made public.

HEU fuel is an important source for PROSPECT since the ^{235}U fission fraction always remains above 99% [20], allowing us to make a direct comparison to ^{235}U spectrum model predictions. The antineutrino spectrum from the reactor is formed by the cumulative sum of all the antineutrinos produced during the beta decay of nearly 800 fission fragments to a flux of $\sim 10^{20}$ $\frac{\bar{\nu}_e}{s}$. This type of flux can not easily be obtained at an accelerator facility and is a unique characteristic of reactors, in this case, HFIR. Figure 2.6 & 2.7 show the expected antineutrino spectrum from a ^{235}U reactor core, as well as a comparison between the expected spectra of ^{235}U and ^{239}Pu fuels in the 1.8 to 9 MeV range.

Uranium 235 decays asymmetrically in two fragments. During a single fission event about 6 anti-neutrinos are emitted, figure 2.8 illustrates the process. A ^{235}U atom captures a thermal neutron and fissions into a light and a heavy fragment and additional neutrons. A high amount ($\sim$200 MeV) of energy is released in each fission; leaving these fragments highly excited. In their decay process, they will beta decay until they reach equilibrium. An antineutrino will be produced during each beta decay. The next section will introduce the design and detection method for PROSPECT.

2.2 Detector Design

PROSPECT is a large scintillator based antineutrino detector using the inverse beta decay (IBD) method (figure 2.9) for $\bar{\nu}_e$ detection. PROSPECT is designed to answer questions about the reactor antineutrino flux deficit, and study short baseline antineutrino oscillations.

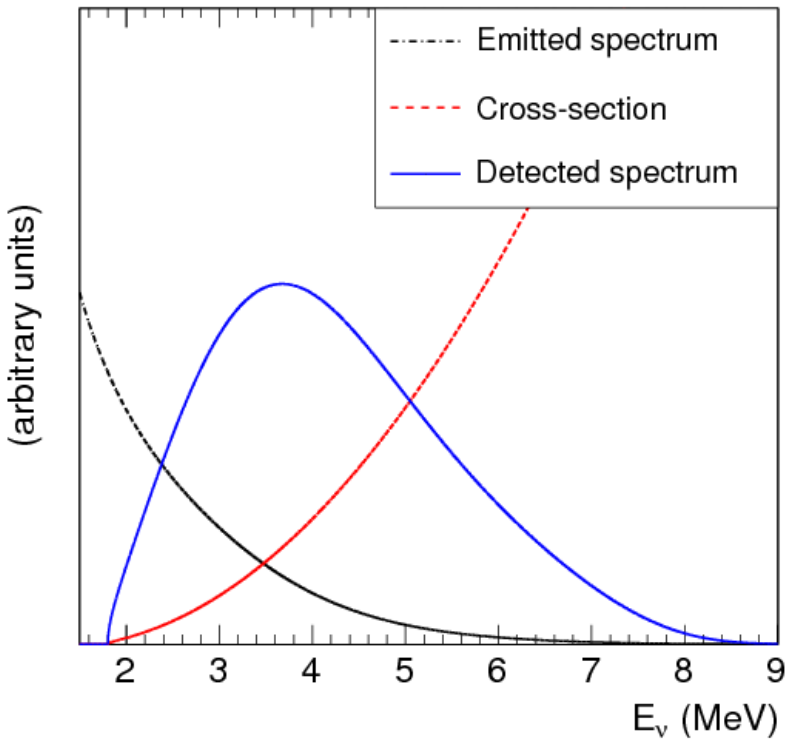


Fig. 2.6: Expected $\bar{\nu}_e$ spectrum.

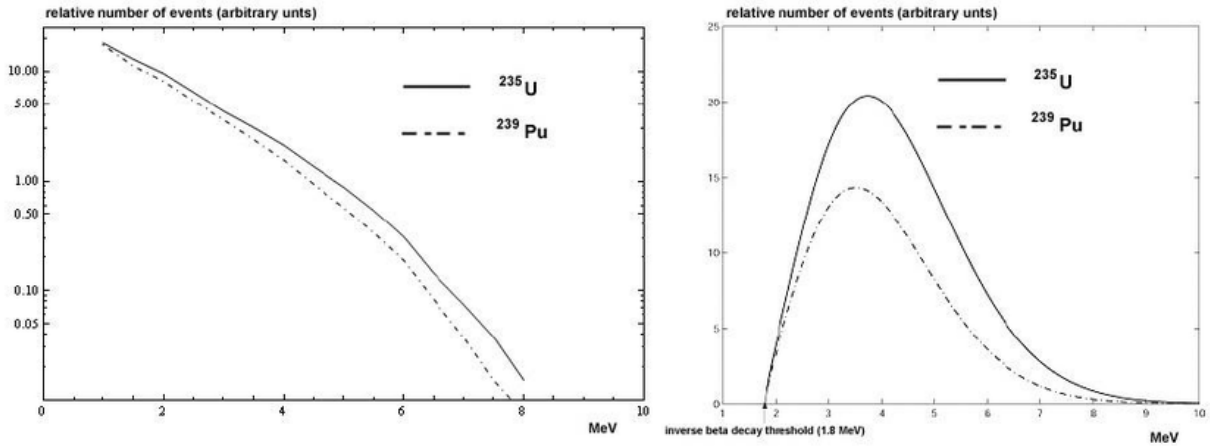


Fig. 2.7: Expected $\bar{\nu}_e$ from ^{235}U and ^{239}Pu.

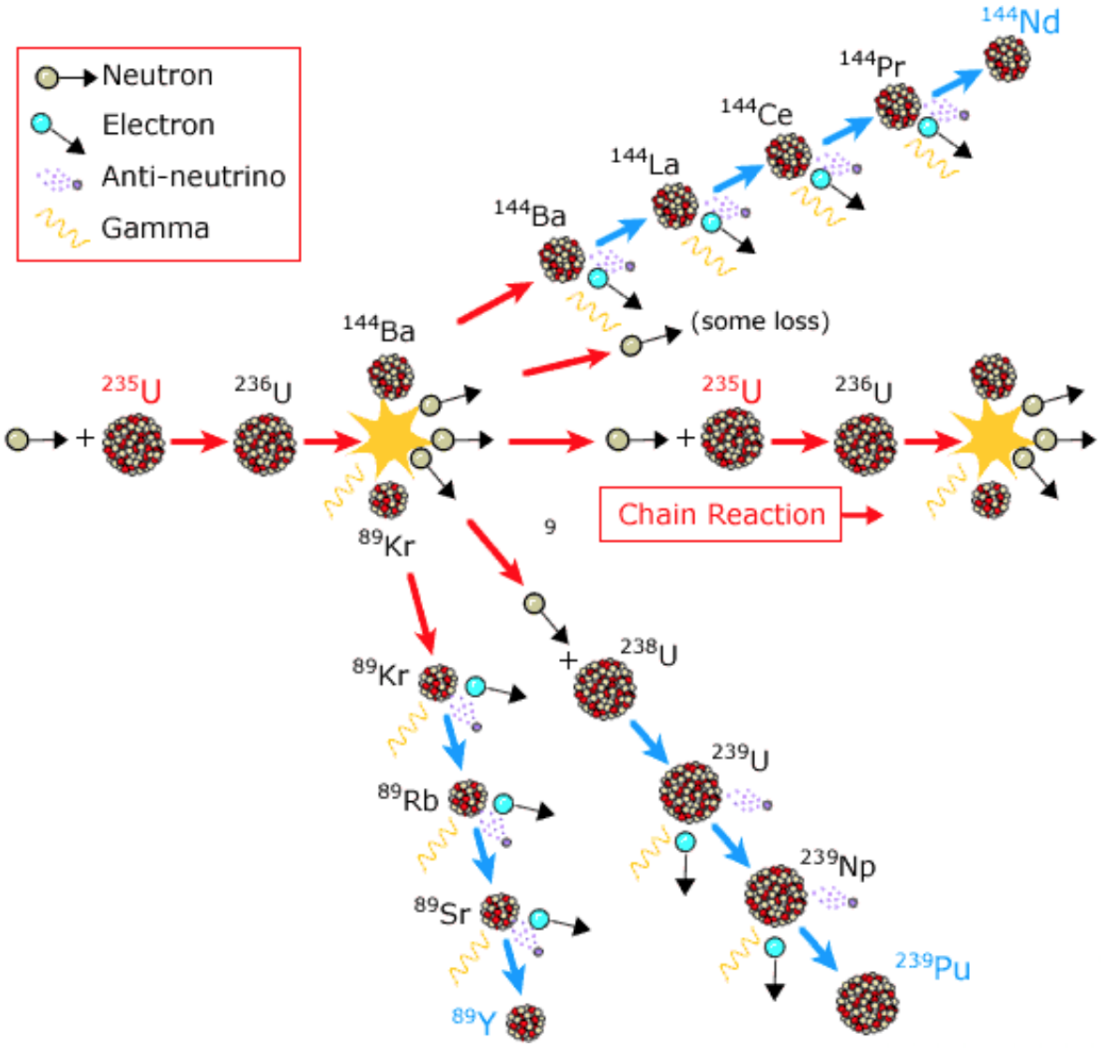


Fig. 2.8: Fission fragments of ^{235}U.

The PROSPECT detector is an 11 × 14 array of optically segmented rectangular segments measuring 1.176 m x 0.145 m x 0.145 m, each one containing two 5 inch photomultiplier tubes (PMTs) for a double-ended readout [21]. In total, there are 308 PMTs from 2 different manufacturers; 240 Hamamatsu R6594 ⌀127 mm and 68 ET 9372B ⌀130 mm [22]. The active detector is filled with ^{6}Li-loaded liquid scintillator (^{6}LiLS) with very good light yield and pulse shape discrimination (PSD) [23]. The detector is shielded with layers of water, polyethylene, borated polyethylene (BPE), and lead to supress γ-rays and neutrons being emitted predominantly from HFIR.

Extensive work has been done at ORNL to establish an understanding of the cosmic muon, gamma and neutron backgrounds prior to the placement of PROSPECT [24]. This work aided the design of the passive shielding around the detector, the shield wall that was installed, figure 2.10, as well as validate the simulation packages on the backgrounds. The shield wall had to be designed, with a floor load limitation of 750 lb/sq. ft, to reduce unwanted IBD-like (2.2.1) coincident events coming from the reactor core.

2.2.1 Method of Detection for Antineutrinos

In the ^{6}LiLS an IBD event is measured by the energy deposited into the ^{6}LiLS from the β^+ ionization and annihilation in inverse beta decay (IBD), $\bar{\nu}_e + p \rightarrow \beta^+ + n$, from which we are able to extract $\bar{\nu}_e$ energy information. An IBD event, figure 2.9, is identified when a delayed signal ($\sim 40\mu s$) from the neutron capture on ^{6}Li is measured in coincidence with the initial β^+ ionization and annihilation signal in the energy range of interest between 1.8-10 MeV [2]. The liquid scintillator used is based on EJ-309 [25], a commercially available liquid scintillator, with ^{6}Li loaded due to its ability to capture an incoming neutron with its large cross section [23].

2.3 Background Environments in Neutrino Physics

Experiments that face very different background conditions in neutrino physics, are the searches for neutrinoless double beta decay in the Majorana [26] and GERDA [27]

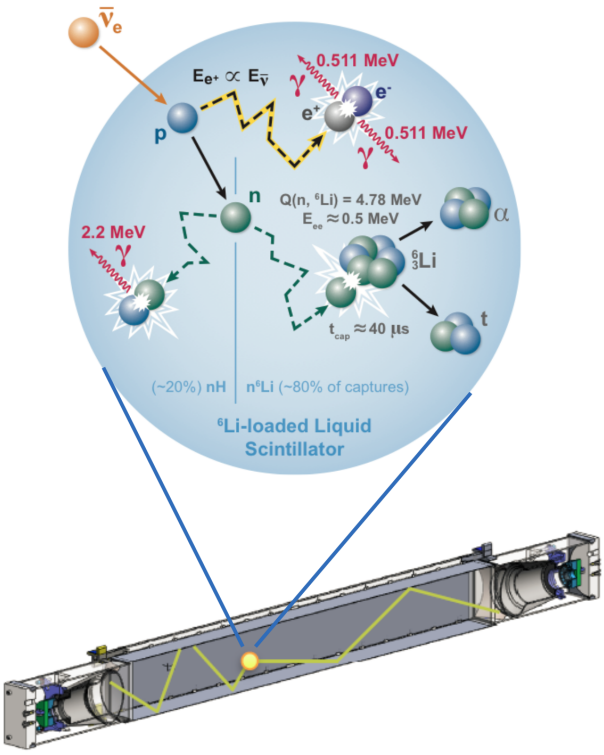


Fig. 2.9: Inverse Beta Decay Process.

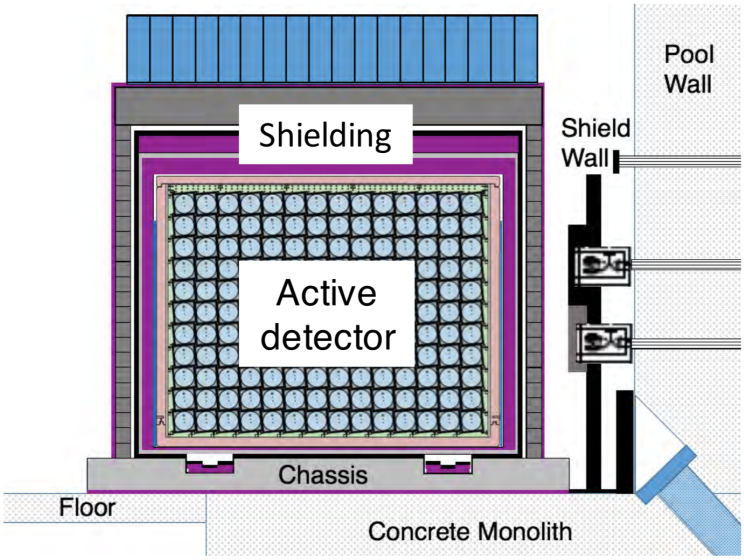


Fig. 2.10: Cross-sectional view of PROSPECT showing segmented active detector and shielding placements.

experiments. The discovery of this very rare decay mode would be the most important result in modern physics [28]. It will give information as to whether the $\bar{\nu}_e$ is a Dirac, or Majorana particle. In the Majorana Demonstrator for neutrino-less double beta decay [26], the background event rate must be as low as possible for a measurement. This is achieved by installing the detector in the Sanford Underground Research Facility (SURF) in a ultra-clean environment where cosmogenic events are minimized and using ultra pure materials to support and surround the detector [29].

The PROSPECT detector does not have the advantage of operating underground, it is operating on the surface level of a research reactor facility with less than one meter-water-equivalent of concrete overburden. The primary backgrounds for PROSPECT come from time-correlated signals from cosmogenic neutrons [2]. Cosmogenic events are estimated by applying the IBD selection to reactor-off data and correlations with the atmospheric pressure differences [30]. We limit the background IBD signal by applying various cuts to event topology to provide two to three orders of magnitude in background suppression [2]. This process is illustrated in figure 2.11. The background environment must be carefully considered to ensure a precise measurement from the detector. In the next chapter, we focus on the magnetic backgrounds from the neutron scattering community near the PROSPECT detector.

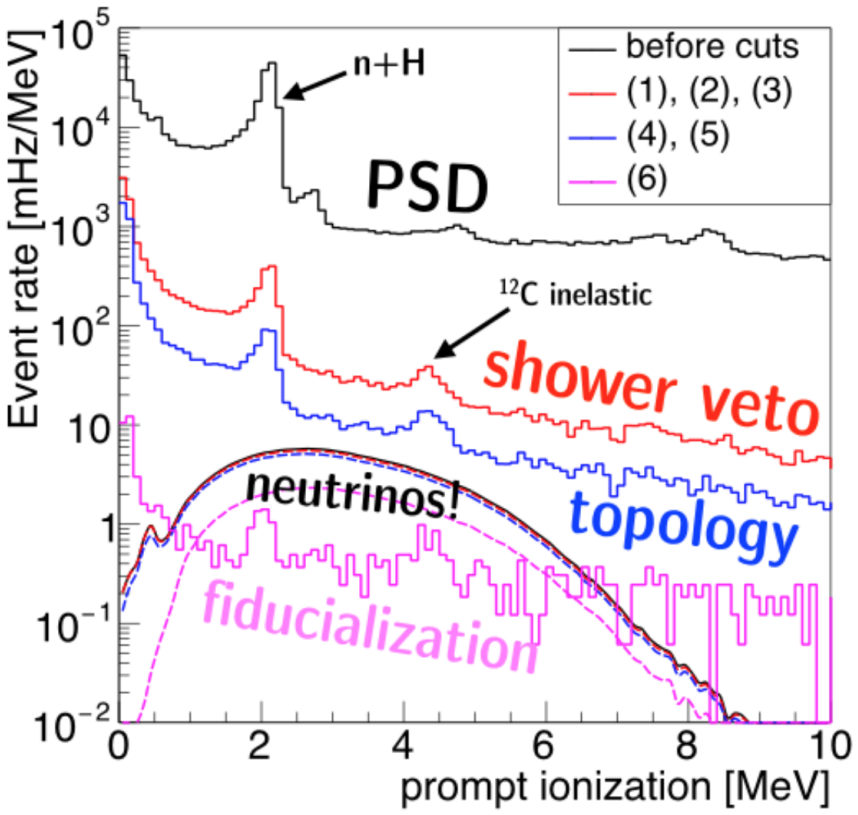


Fig. 2.11: Simulated signal and background spectra. Background is primarily from cosmogenic fast neutrons. Cuts are applied based on IBD timing and spacial characteristics. Adapted from [2].

Chapter 3

Magnetometer System

3.1 Introduction

The main purpose of HFIR is to provide a high-flux source of neutrons to the various neutron scattering instruments located one floor below PROSPECT. Figure 3.1 shows the approximate location of the PROSPECT detector one floor above the experiment hall, in red, as well as the location and various instruments used in the experiment hall.

As a research reactor, HFIR provides several different magnets and cryogenic sample environments for the neutron scattering community. Magnets ranging from field strengths of 5 to 11 Teslas (T) can be used on various beam-lines throughout a run period. Beam-line 3 (HB-3) is almost directly below the detector, and is able to use magnetic field environments in the 5 T to 8 T range. HFIR provides 5 T and 6 T vertical symmetric field magnets, 8 T and 11 T vertical asymmetric field cryomagnets, and an 11 T horizontal field magnet. Improvements to the magnetic sample environments have been discussed by the neutron scattering community. It is expected that work will be done in the future to incorporate magnetic environments 2 to 3 times stronger than what is currently available [31].

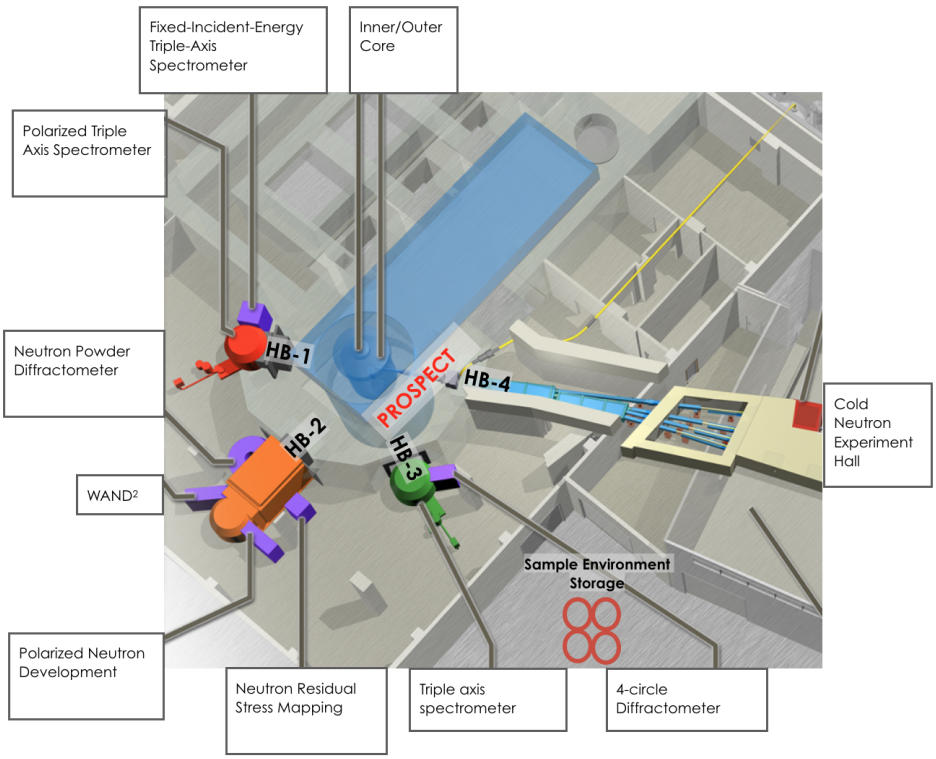


Fig. 3.1: Experiment hall at HFIR.

3.2 Magnetic Backgrounds

In 2016, the background magnetic fields were mapped at HFIR before the PROSPECT detector was in place. The results showed magnetic field magnitudes up to 2 Gauss during the operation of the high strength magnetic environments in the experiment hall [32]. Similar studies have been conducted in other experiments such as the STEREO neutrino experiment [33], where the entire detector was shielded from the magnetic background of high magnetic field experiments conducted nearby. Other experiments in physics require the suppression of magnetic backgrounds around the PMTs, such as the DAMPE dark matter experiment [34] and the GRIS and PING-M space experiments [35]. The effect of the magnetic field on the PMT is well known and has been studied directly on different types of PMTs [36].

3.2.1 Magnetic Field Effects on Photo Multiplier Tubes

A PMT takes in an incoming photon, and through the photoelectric effect it produces an electron that is sent to a dynode configuration for amplification on the order of 10^6. When the photoelectron travels from the photocathode to the electron dynode configuration, a slight magnetic field could distort its trajectory. With fewer electrons hitting the dynode configuration, the less the signal is amplified, resulting in a smaller gain than what would be expected. The distortion of the trajectory could also effect the timing and pulse shape of the PMT. Modern PMTs are designed and optimized for efficient secondary electron collection. In some cases, the timing performance of the PMT might be a crucial for the specific application. The effects have been studied where the reported plot of the gain versus magnetic flux density is shown in figure 3.2 using a ⌀13 mm head-on PMT [37].

Figure 3.3 shows the gain variation of the Hamamatsu R6594 PMT with respect to the magnetic flux density in Gauss. With a 2 Gauss field applied, the relative gain output of the PMT studied dropped 80% with magnetic shielding [32]. These results made us conclude that we need careful monitoring of the magnetic environment around PROSPECT by implementing a system of magnetometers into the environmental monitoring slow-control server. The superconducting magnets used on the neutron scattering beamlines are not being used continuously, so it is important to be aware of when a on is being ramped up near the detector. Figure 3.4 shows the current magnet operation since PROSPECT has been commissioned at HFIR.

3.2.2 Magnetic Shielding

A common technology used to reduce the effect of magnetic fields on sensitive equipment is the use of a soft ferromagnetic alloy with very high permeability surrounding the equipment low static or slowly varying fields. The high permeability of the material acts as a sponge for the magnetic fields to redirect the field around the shielded volume.

To help reduce the background magnetic field effects, PROSPECT uses a Hitachi FINEMET magnetic shield that is fitted around each PMT. Figure 3.5 shows a 5 in. PMT, and figure 3.6 shows a drawing of the PMT in a cell fully assembled. The Hitachi FINEMET

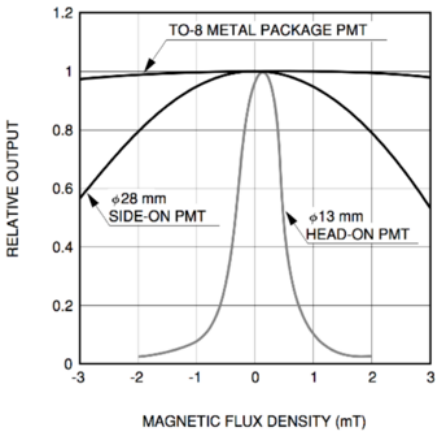


Fig. 3.2: Relative output of Hamamatsu ⌀13 mm head-on PMT without magnetic shielding [37].

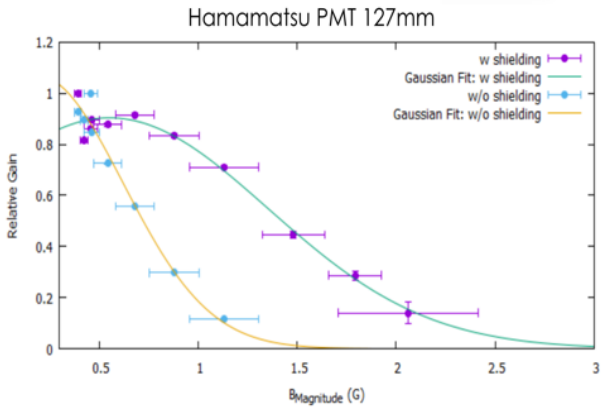


Fig. 3.3: Relative gain of Hamamatsu ⌀127 mm head-on PMT with and without magnetic shielding surrounding the photocathode [32].



Fig. 3.4: Schedule of magnet operation on each beamline during the operation of PROSPECT.

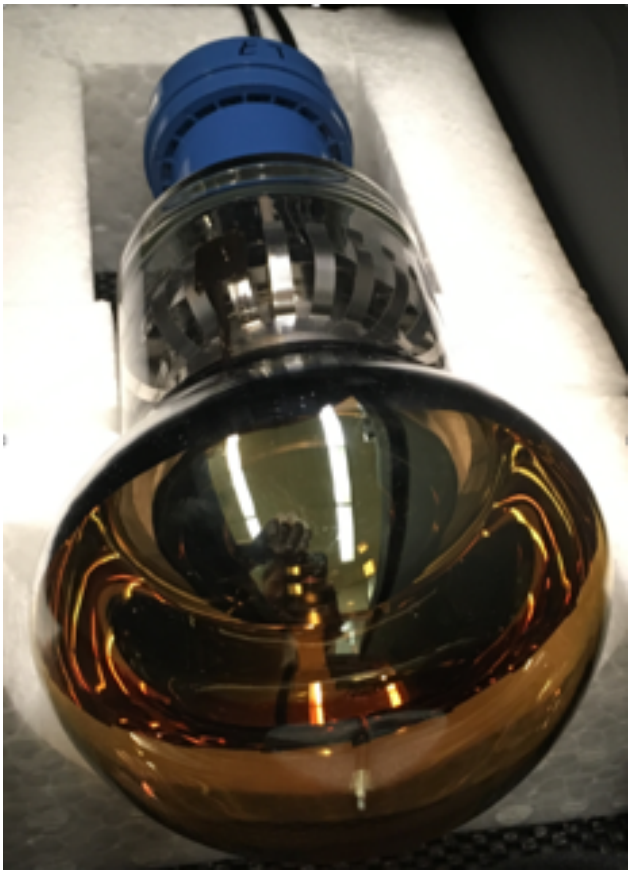


Fig. 3.5: ET 9372B PMT.

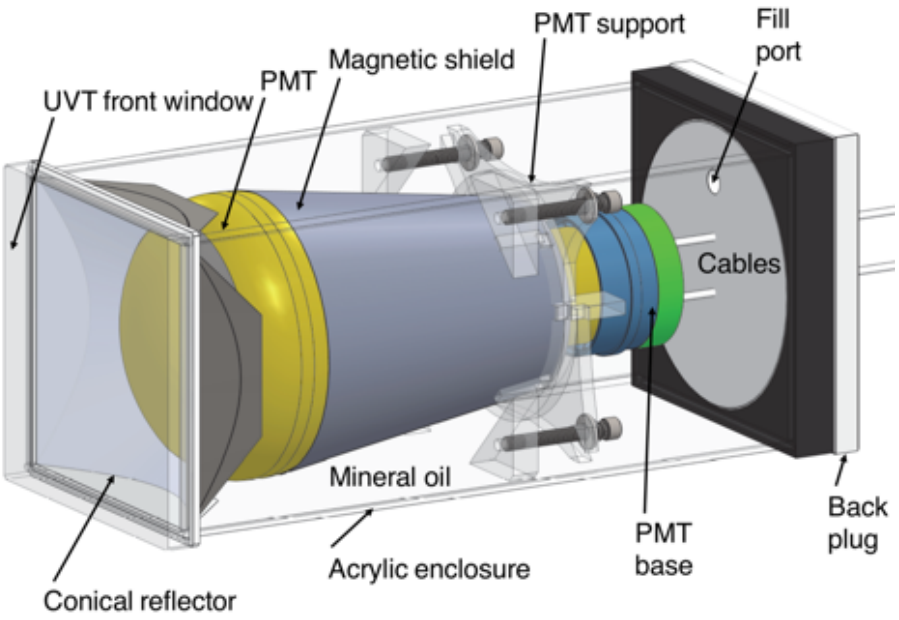


Fig. 3.6: PMT cell setup inside The PROSPECT Detector.

shield is an amorphous metal composed of Nb, B, Fe, and Cu with a high permeability and higher saturation flux density compared to various other materials. The high saturation flux density allows the magnetic shield to withstand higher magnetic fields, in the 1 to 1.5 Gauss range for a single layer shield [38]. Preliminary studies on the effectiveness of the magnetic shielding have been conducted and have shown that the shielding increases the PMTs resistance to magnetic flux, as shown in figure 3.3. The gain of the Hamamatsu ⌀130 mm PMT dropped to nearly zero in the 2.5 to 3-Gauss range, even with the shielding applied.

3.3 Design of a Magnetometer System

A simple to use and cost effective monitoring system has been developed using a Raspberry Pi and Adafruit sensor boards for measuring the background magnetic field.

3.3.1 Raspberry Pi

The Raspberry Pi (RPi) is a very compact single board processor computer. The RPi model 3b processor is a quad Core 1.2 GHz Broadcom BCM2837 64bit CPU and has 1 Gb of RAM. This powerful device can be used as a desktop computer with an HDMI monitor, or it can be used in a similar fashion to a micro-controller. The RPi is convenient for this project because of its ability to function as a standalone computer in an internal network. The RPi easily connects to the local network of computers in the PROSPECT data acquisition setup and is accessible outside of the network. This allows a user to connect to it remotely to perform tasks on it, such as updating the code, or collecting the data.

3.3.2 I^2C Introduction

I^2C communication protocol allows the communication of a "slave" chip (magnetometer) with a "master" chip (Raspberry Pi) over short distances, and requires the use of only 2 signal cables, SDA (data line) and SCL (clock line). With two wires and a proper multiplexer,

a single "master" chip can communicate with up to 1008 devices with transmission rates of either 100 kHz or 400 kHz.

To begin a request, the "master" chip drops the SDA signal to low then the SCL signal drops to low, to prepare the "slave" chip for the incoming transmission. The 7 address bits tell the "slave" which device it wants to talk to. The 8^{th} bit sent by the "master" indicates a read or write operation. The 8 data bits are then either sent to or collected from the "slave" chip, depending on read or write request, before the stop condition is signaled. This process is drawn out in figure 3.7.

3.3.3 Magnetometer Chip

The Adafruit LSM303DLHC Triple Axis Magnetometer board (0.9 cm x 0.8 cm) comes with the LSM303DLHC 3D magnetometer 3D accelerometer chip developed by STMicroelectronics. This chip uses the Hall Effect to measure small fields within 8.1 Gauss, and has a selectable range of measurement from 3.1 to 8.1 Gauss by changing the LSB/Gauss conversion factor in the sensor library setup code. The output voltage of the chip is read by the RPi as Least Significant Bits (LSB), and that is converted to Gauss by a constant given in the LSM303 data sheet.

This chip operates on low power (2.16 to 3.6 V). The magnetic resolution is 2 mGauss with a 10000 Gauss maximum readable field. A field above the maximum readable field will distort the performance and the sensor will need to be reset and re-calibrated.

The advantage of the Adafruit board is that the sensor is soldered onto a board with pre-soldered pull-up/pull down resistors, and is ready to use. The pull-up/down resistor is necessary for some chips to ensure that the state is well-known in the signal. For this sensor, two pull-up resistors are necessary on the inter-integrated circuit (I^2C) lines that carry the signal to the Raspberry Pi, or micro-controller (Arduino). These pull-up resistors allow the chip to send data fast (between 100 and 300 ns) [39].

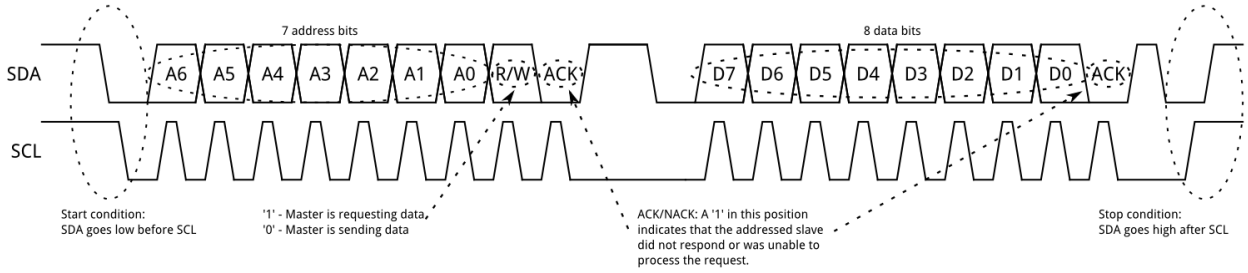


Fig. 3.7: Basic transmission of request and response over I^2C communication protocol.

3.3.4 Multiplexer

Since a Raspberry Pi has only one set of I^2C lines available, it is necessary to configure a multiplexer to connect more than one sensor to a single Raspberry Pi. The Adafruit TCA9548A I2C Multiplexer uses the TCA9548A multiplexer chip from Texas Instruments with the necessary pull-up resistors pre-soldered on the board, making this another easy chip to install. The multiplexer allows up to 8 different devices with the same I^2C address to be connected to a single micro-controller, and easily switch between them in the program.

3.3.5 I2C Signal Extenders

The downside to I^2C communication is that the signal transmission length is limited to a few cm before electrical interference distorts the signal. One way to resolve this issue is to split the signal into two separate lines (differential I^2C (dI^2C)) for each the sda and scl lines to sda+, sda-, scl+, and scl-. The Sparkfun I^2C Bus Extender is based off of the PCA9615 chip from NXP Semiconductors. This chip is able to convert the I^2C signal to dI^2C, send each component of the signal over 4 lines in an ethernet cable, and convert back to I^2C on the other end of the transmission line. For this project, There are 2 I^2C signal extenders for each sensor. One attached directly to the magnetometer and the other attached close to the I^2C multiplexer. This gives the freedom to transmit data from the magnetometers up to 100 feet.

3.4 Magnetometer System Setup

The RPi is connected to the slow controls ethernet switch inside the PROSPECT DAQ rack. The RPi collects the data from each magnetometer every quarter-second for one minute and averages that data for database storage. The data collection program and averaging program are all written in python and can be viewed in the Github Repository for this project [40]. The averaged data is sent through a socket communication protocol to the PROSPECT slow control server and is plotted and stored there for monitoring.

3.4.1 Slow Control Communication Protocol

The slow control server and the RPi are able to talk to each-other through a network socket communication. The RPi is programmed to listen to a specific port number on the local network that the slow control server has access to. The slow control server is then programmed to send the RPi a request for sensor data from any one of the six sensors at a time. Once the RPi receives that request, it is then programmed to look for the most recent averaged data from the sensor of interest and send it back to the server. This data is then stored in the slow control database, plotted and then can be viewed internally by anyone in the collaboration, figure 3.8.

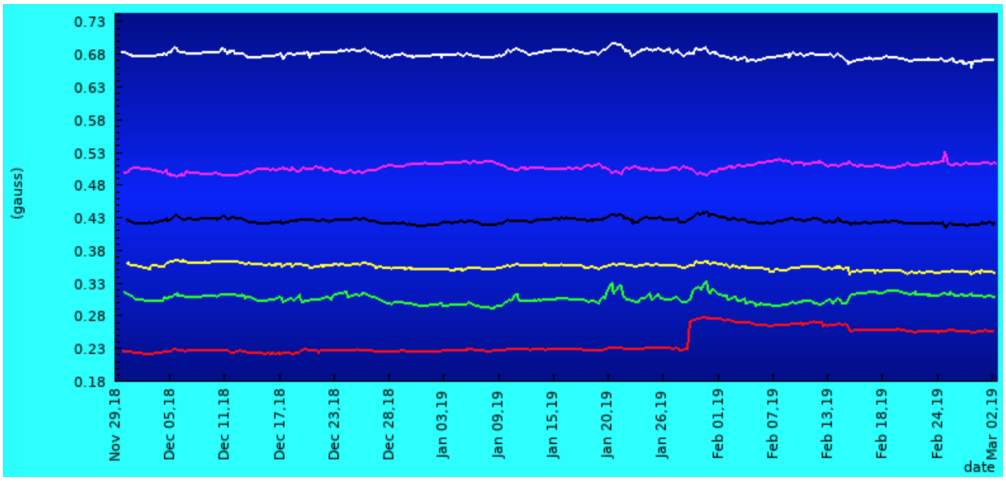


Fig. 3.8: Screenshot of the slow control server live plots.

3.4.2 Deployment Around PROSPECT

There are a total of six sensors placed strategically around PROSPECT, see figure 3.9 & 3.10. One sensor is placed in each corner, near the PMTs, and one in the center of the 1.19 m long call between the PMTs. The Raspberry sits in the DAQ rack shown in the figure, and 20 ft of cat 6 ethernet cable is routed to each one of the sensors. Any extra cabling is coiled up behind the DAQ rack.

The chassis of PROSPECT is made up of ferromagnetic materials; this was taken into consideration before determining the height of the sensors above the chassis. Figure 3.11, shows the magnetic field at various heights above a magnetic 'hotspot' on the chassis. The hotspot drops from 1.170 Gauss at 0.0 cm above the chassis to 0.490 Gauss (Earths magnetic field background at ORNL) at 10 cm above the chassis [41]. Each sensor is centered at about 14 cm above the chassis, where the center of the first layer of PMTs is approximately 2 cm higher. Figure 3.12 shows the placement of the sensor on the lid of the custom designed 3D printed box that is affixed to the detector.

3.5 Calibration

The magnetometer chips must be re-calibrated after being disconnected from power. In order to properly calibrate them, a good resolution hall probe calibrated in a zero gauss chamber is used. There are two available hall probes, a single-axis highly sensitive Lakeshore hall probe and a triple-axis Metrolab hall probe. All the calibration programs for this system were written in python and can be found on the github page for this project [40].

3.5.1 Lakeshore Hall Probe

The Lakeshore single-axis hall probe (Model #: HMMT-6J18-VF) is a 305 mm hall probe that must be used with a Lakeshore 475 Gaussmeter and can be read to a computer through a serial communication port. The total system is bulky and the probe is very fragile due to its length and thin material composition. This hall probe can read in a variety of ranges

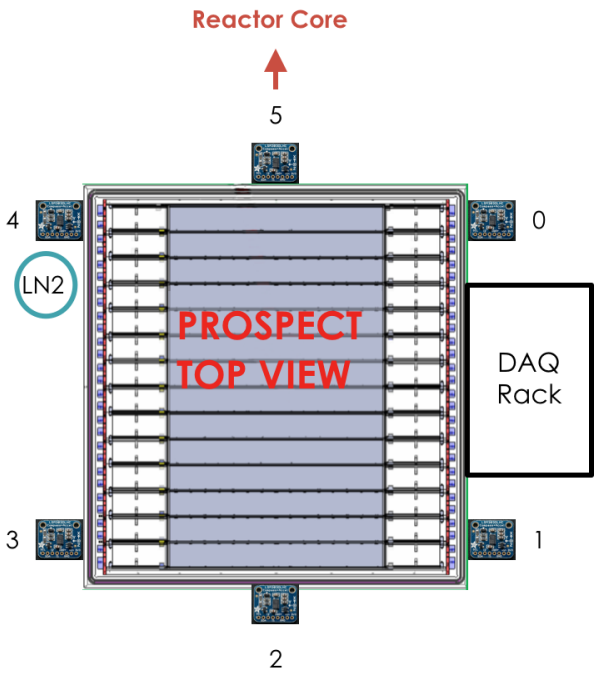


Fig. 3.9: Position of the sensors attached to the detector.

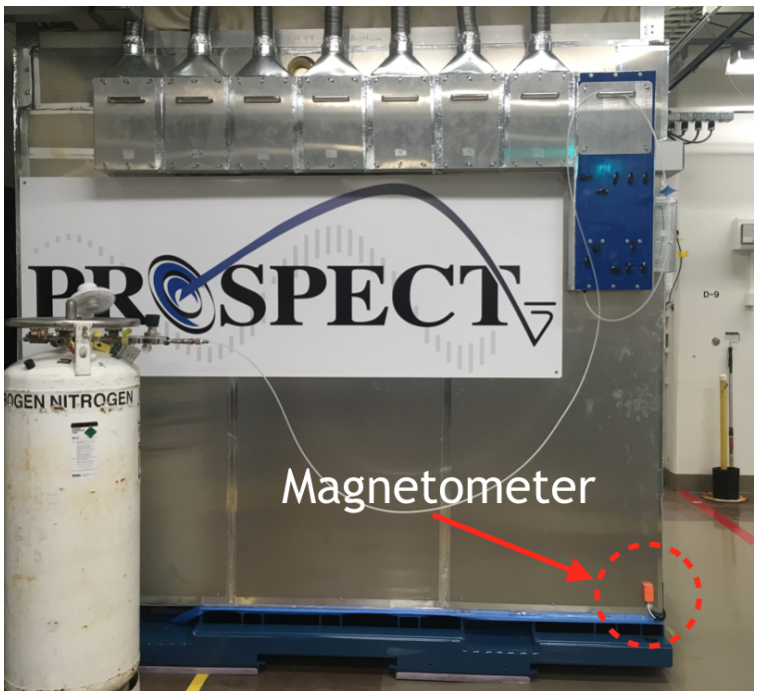


Fig. 3.10: Photo of Magnetometer attached to PROSPECT.

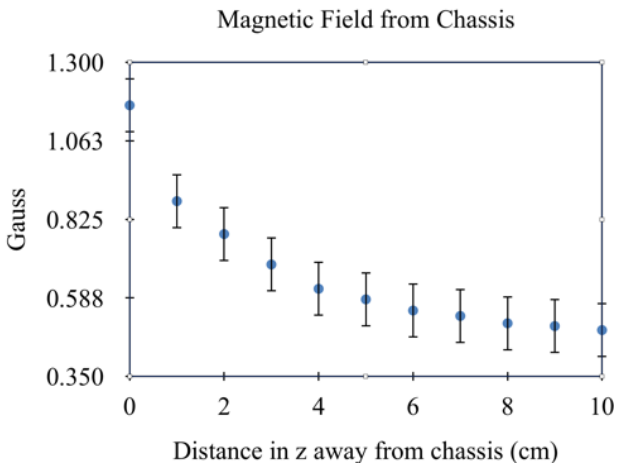


Fig. 3.11: Z scan of the magnetic field from magnetized chassis using the Lakeshore single-axis hall probe.



Fig. 3.12: Photo of the lid with a magnetometer attached.

from ±35 Gauss to ±35 kGauss with an accuracy of ±0.1%. The probe was calibrated in a zero gauss chamber (Model #: 4060) before each use. The hall probe and zero gauss chamber can be seen in figure 3.13.

3.5.2 Metrolab Hall Probe

The Metrolab triple-axis hall probe (Model #: THM1176-LF) is more robust and simple to use. This particular model is for low-field measurements in the ±8 mT or ±80 Gauss range. This hall probe easily communicates to a computer using a Labview interface provided by the manufacturer and a usb connection. This is the prefered measurement device since it is much less fragile, less bulky, and simpler to program. This device comes factory calibrated and requires calibration every 6 months in the provided zero gauss chamber and calibration program. This probe can be seen in the 3D printed mount in figure 3.14.



Fig. 3.13: Lakeshore hall probe and zero gauss chamber for calibration.



Fig. 3.14: Metrolab hall probe in custom 3D printed stand for calibration.

3.5.3 Calibration Program

For a magnetometer to be properly calibrated, the x-, y-, and z-axes measurements must be the same in magnitude when the chip is aligned along either the + or the - of the same axis in a static background magnetic field. For example, in a field directed along the x-axis with a magnitude of 1 gauss, the magnetometer should read +1 gauss and -1 gauss when aligned along the +x- and -x-axis respectively. This type of calibration will be referred to as the axes-shift calibration.

The axes-shift calibration is done by simply running the calibration program and rotating each sensor in 3-dimensions about the center of the board until all the maximum and minimum values recorded on the terminal screen stop updating. The program will collect the maximum and minimum values read for each axis of the magnetometer and take the average. If properly calibrated, the average value should read zero, otherwise it will print out the shift necessary to calibrate that specific axis. This process can be seen in figure 3.15

and 3.16. These figures show a 2D case of the axis shift calibration, where you can see the x- and y-axis magnetic field values plotted as coordinates before and after calibration. After calibration, it is easy to see that the circle of values is centered about the origin, indicating that the magnitude of the magnetic field is the same in every direction. This process takes about 2 minutes to complete for each sensor.

Once the axes-shift calibration is complete, the magnitudes of each sensor must be scaled to match a known value. One of the hall probes described in sections 3.5.2 & 3.5.1 is used as the known value for the magnetic backgrounds. Each sensor is measured for 1 minute and compared to the one minute average value of the hall probe. The average magnitude in each the x-, y-, and z-axes are then scaled on the Adafruit magnetometers to match the hall probe. The next section will discuss measurements made around PROSPECT with both the hall probes and the calibrated Adafruit magnetometers.

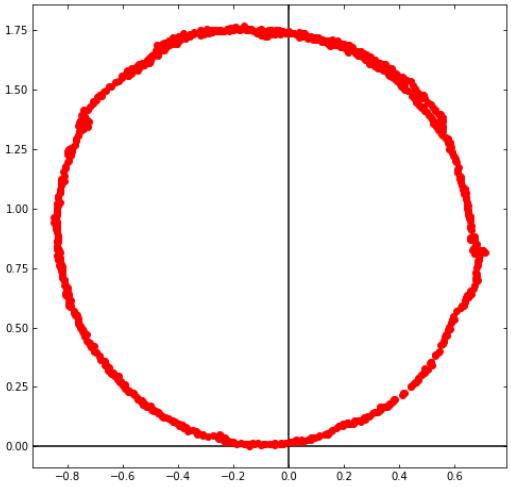


Fig. 3.15: x- and y-axis magnetic field plotted before axes shift calibration.

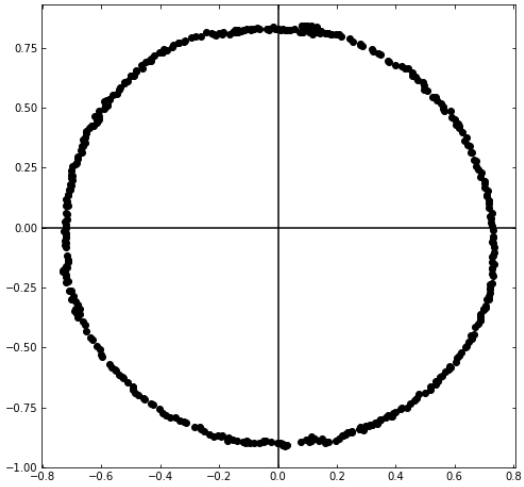


Fig. 3.16: x- and y-axis magnetic field plotted after axes shift calibration.

3.6 Measurements

3.6.1 Mapping Around the Detector

The triple axis hall probe from Metrolab has been used to map the field around the detector in 5 cm increments at the height of the magnetometers. The 3D plot, figure 3.17, shows a 10x amplified magnetic background magnitude to make the direction of the vectors more clear. Figure 3.18 shows a heat map of the magnitude of the background field. The highest background magnetic field is measured next to the data acquisition rack caused by the electronics.

3.6.2 Bench Tests for Stability and Calibration

A bench test calibration was made where each sensors was compared to the known value from the Lakeshore Hall probe. The sensors were grouped together and calibrated in the same background field to demonstrate how the sensors compare when reading the same value. The initial spread in readouts of the Adafruit sensors is about 0.5 Gauss before calibration, after they are calibrated, the sensors matched with a less than a 0.15 Gauss spread; this is presented in figure 3.19. The stability of the sensors during an overnight measurement are shown in figure 3.20, the jump at the very end corresponds to a computer being placed near the small cluster of sensors. Some of the sensors read a higher jump and some read a lower jump in magnetic field, due to the x and y measurement axes being inverted between two groups of three sensors.

3.6.3 Measurements Around PROSPECT

Shortly after placing the sensors around the PROSPECT Detector, a test was conducted with Mag-E, the 8 T vertical field cryomagnet. This test took place over an hour and the magnet was ramped-up and down manually before beam-line operation. There is no recorded data of the exact field that was produced by this magnet during this test, however it was confirmed that the spike shown in Figure 9 on November 5 correlates to the time in which

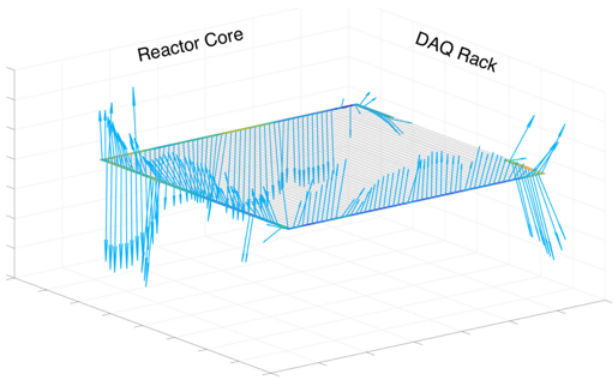


Fig. 3.17: Angled view of PROSPECT detector with magnetic field vectors plotted around the edge.

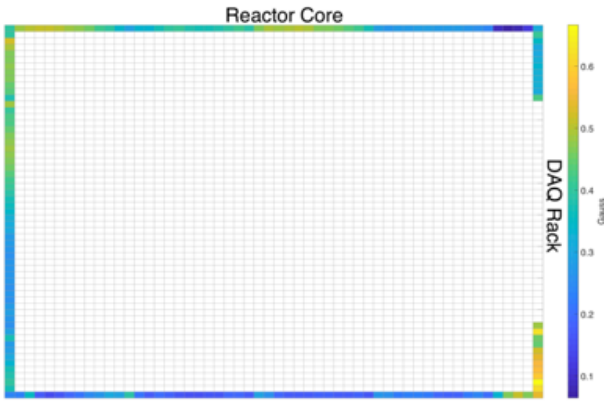


Fig. 3.18: Top view of the detector with magnetic field magnitude plotted as a heat map along the edges.

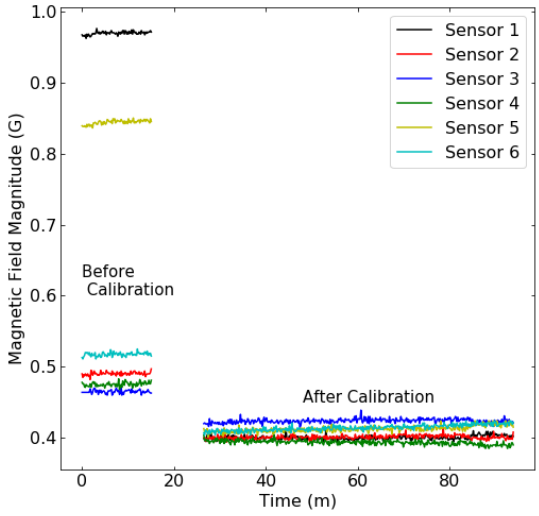


Fig. 3.19: Magnetic field measured by 6 sensors before and after calibration in a static magnetic background.

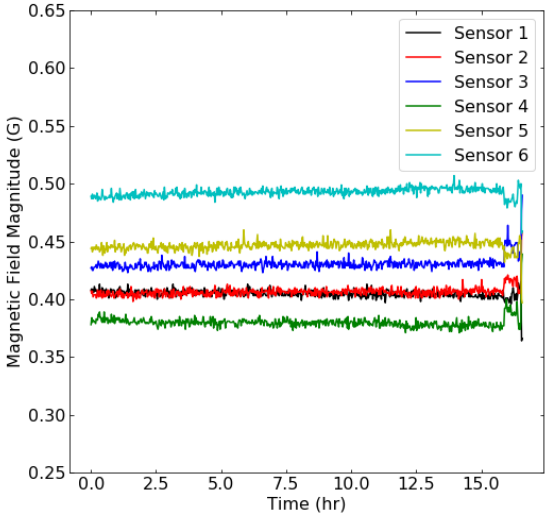


Fig. 3.20: Overnight stability of magnetometers after calibration.

the test was conducted. The spike that was seen by this system of magnetometers exceeds 1 Gauss for one of the sensors, see figure 3.21.

3.7 Conclusions with Magnetometers

The PROSPECT detector is located at HFIR at Oak Ridge National Laboratory. This research reactor can potentially have high magnetic field backgrounds that may affect the PMTs of the detector. We have developed a compact, low-cost magnetic monitoring system using Adafruit triple-axis magnetometers. As a first step, we have designed a remotely-operated monitoring system of six sensors surrounding the detector. The sensors have been calibrated and have shown stability and accuracy with less than a 0.15-Gauss spread. The location of the sensors has been selected at the edge of the bottom of the first layer of PMTs. These locations have been surveyed with a triple-axis hall magnetometer from Metrolab, having a magnetic fields less than 0.7 Gauss. The sensors are fully operational and fully integrated into the slow controls and will be actively monitored by the collaboration during normal operations. This simple and inexpensive array allows us to monitor magnetic field conditions that could affect PROSPECT by integrating the environments magnetic background data into the slow control system. An array like this can be easily adapted to other experimental setups that require spatial and temporal monitoring of magnetic fields.

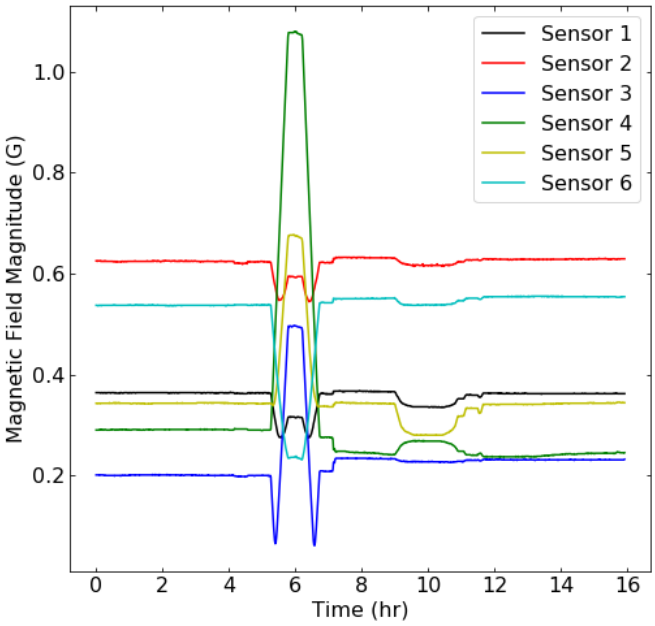


Fig. 3.21: Each sensor around PROSPECT reacting to the testing of Mag-E on HB-2A.

Chapter 4

Gamma Scanning Project

4.1 Introduction

The High Flux Isotope Reactor (HFIR) "is the highest flux reactor-based source of neutrons for research in the United States [18]". Along with the PROSPECT experiment, 4 beamlines containing 16 instruments all benefit from the high neutron flux of the compact highly enriched Uranium-235 (HEU) core. However, an unplanned shutdown in November, 2018 [42] motivated the exploration of gamma ray detector technology as a diagnostic tool for reactor fuel elements. Based on technology used at the Advanced Test Reactor (ATR) at Idaho National Laboratory (INL) [3], an experimental setup was implemented to allow operation of gamma detection equipment underwater. With a system that can withstand high doses of radiation and inspect the gamma signatures in a small area, a passive assay of the fuel core can be obtained.

4.1.1 Detector Housing

The detector housing is a well-designed system for providing the ability to take gamma spectra measurements in an underwater environment. The main body of the detector housing is an aluminium cylindrical shell with o-ring sealed caps on either end of the cylinder. The housing contains large amounts of bismuth for shielding, with an interchangeable collimator to change the viewing area as needed. The shielding for the detector was milled to be able to

hold 4 different gamma ray detectors; a high purity Ge (HPGe) detector, a LaBr3 scintillation detector, a high pressure xenon (HPXe) detector and a room-temperature CdZnTe (CZT) detector. Wiring for the detectors is fitted into a 3/4 inch port in one of the end plates with an attached EVA tube to bring the cables out of the water. A custom cable was designed for this purpose to incorporate different signal cables for each detector, and high voltage supply. Figure 4.1 illustrates the components of the detector housing discussed above. Initial testing of this setup took place in a clean testing station in order to ensure that everything was operational and properly installed.

4.2 Detector Testing Station

The testing station was implemented at the Physics Division at ORNL to provide an 'offline' location to perform extensive testing on the detector housing and detectors. The station

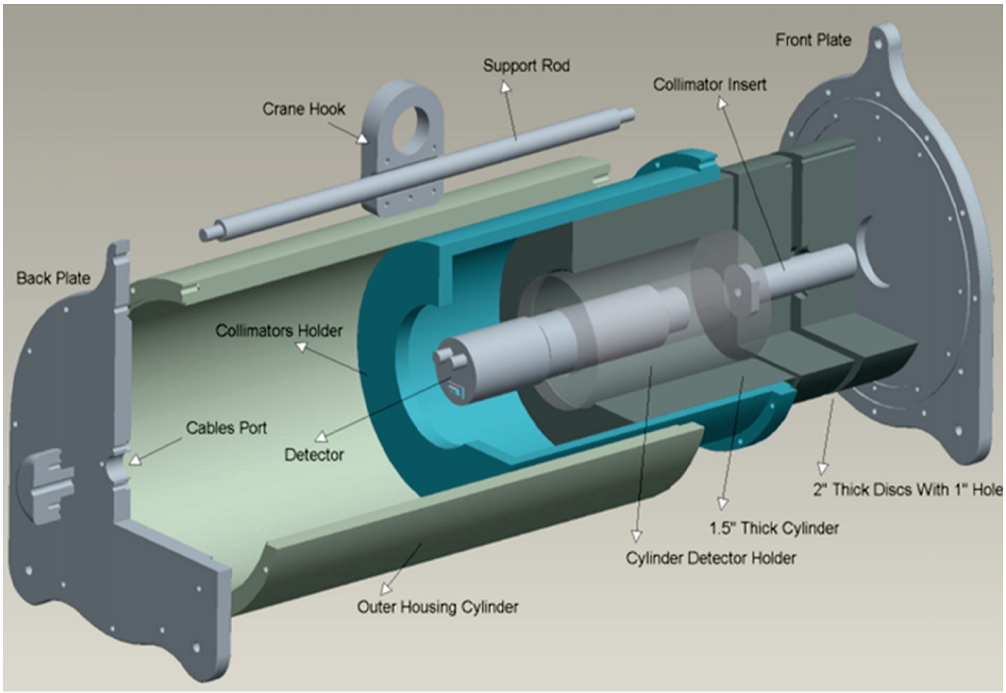


Fig. 4.1: Underwater gamma-ray detector housing [3].

has a 1500 gallon plastic container (73 in. W x 84 in. H) filled with water to provide enough pressure to perform leak tests on the detector housing (figures 4.2 & 4.3). A gantry crane with a chain hoist was used for the safe lifting and movement of the ∼200 lb housing inside the bucket. The gantry crane spans the diameter of the bucket allowing easily controlled movement from side to side as well as vertically while the housing is submerged.

With the ability to move the detector horizontally, close to the wall, an external source can be placed outside of the bucket and studies can be performed on the effects of water attenuation on the signal. These studies would help determine how the signal of the detectors change as we add more water between it and the source.

The testing station allows us to experiment with different methods to orient the housing and which type of tubing would be easy to move, yet be rigid enough to keep water from leaking into the cable port. Three different types of tubing were considered: Ethyl Vinyl Acetate (EVA), flexible EVA, and high density polyethylene (HDPE). The HDPE was used first and was too rigid for this project. The tubing did not allow the detector housing to be moved freely while submerged. The EVA tube was then tested and found to be much more manageable while moving the detector housing. The bending radius on the EVA tube is 4 inches, compared to 10 inches bending radius for the HDPE. This more flexible tubing will also not put as much strain on the o-ring sealed points of entry when trying to position the system.

The detector housing is designed to be water-proof and has only 3 points of entry for water if not properly sealed; the front and back plate's o-ring seal, and the cable port seal. While the housing was empty we were able to practice removing and re-installing the back-plate, which is necessary to change detectors or collimator. The seals performed well and everything was re-installed properly. There were 2 instances where the o-ring seal was not properly aligned and this resulted in a small leak into the detector housing. A leak detection system has been implemented into the housing and we were able to detect this leak quickly. Operating in an environment like HFIR, with high radiation and risk of contamination, the detection housing requires a leak detection method inside of the housing to determine if a seal has been compromised and the detectors can be operated safely. The next section will introduce the various choices of gamma-ray detectors.



Fig. 4.2: Corey, Dr. A Galindo-Uribarri and the 1500 gallon bucket.



Fig. 4.3: View of the housing submerged in the bucket.

4.3 Choice of Gamma Ray Detection Technology

With several choices of gamma-ray detectors available, we narrowed down our decision based on some key characteristics that were required for this project. The detection method needs to be robust, be reliable, withstand a harsh environment with strong radiation fields, have good resolution, be thermally stable, have the adequate detection efficiency, and be able to detect gamma-rays in the range of interest of up to ∼2 MeV. The detector also needs to be directional, but the heavy collimation in the housing focuses the detectors field of view.

The different types of gamma ray detectors that were considered were scintillator-based and semiconductor detectors. The scintillator-based detectors are a $LaBr_3$ scintillating crystal with a photosensor coupled to the crystal, and an HPXe gaseous scintillator coupled to a photosensor. The semiconductor detectors are a CdZnTe, and an HPGe. Table 4.1 shows the main characteristics of each detector. We narrowed the choice down to the $LaBr_3$ scintillator detector and the CdZnTe semiconductor detector, and finally chose the latter.

Table 4.1: Comparison between different semi-conductor and scintillator based detectors.

Detection Type	Detection Material	Density (g/cm^3)	Energy Resolution @ 662keV	Operating Voltage (VDC)	Comments
Scintillator	$LaBr_3$	5.3	3.3%	-600	-
Gas Scintillator	HPXe	0.4	2.0-2.5%	-4000	-
Semi-Conductor	CdZnTe	6.0	3.1%	-1500	-
Semi-Conductor	HPGe	5.32	0.2%	HV	LN_2 cooled

This decision was based on the lower detection efficiency and better resolution of the CZT detector over the $LaBr_3$. The next section focuses on the method of detection for, and the characteristics of the CdZnTe semiconductor detector.

4.4 Semiconductor Detectors

4.4.1 Semiconductor Gamma Ray Detection Mechanism

Semiconductor gamma-ray detectors work much differently than scintillator-based detectors. A semiconductor detector measures directly the effect of a charged particle incident on the detector, compared to scintillator-based where the radiation must interact with the scintillator to produce light which is then read out by the PMT.

Semiconductors have a very small energy gap, meaning that it requires a low amount energy deposited to create an electron-hole pair (figure 4.4). Ionizing radiation incident on a semiconductor sets free, charge carriers in the detector material by leaving holes in the valence band. These charge carriers are then pushed across the energy gap, creating a voltage gradient in the detector material. This relationship between free charges in the conduction band, and holes in the valence band is known as an electron-hole pair. The voltage difference is then measured by the two electrodes in the detector. The number of electron-hole pairs is proportional to the energy of the incident radiation on the material [43]. The CZT detector

requires a deposition of 4.64 eV to generate one electron-hole pair, this is about 3 times larger than the energy gap [44].

4.5 Cadmium Zinc Telluride Detector

The CZT detector is a good detector and has several advantages over the scintillator-based detectors for this specific project. The detector used was the eV large volume (1000 mm^3) CZT detector. In the region of interest of about 600-800 keV, it is reported by Vo, D. that the CZT has a slight advantage in the full width at half peak maximum (FWHM) of about 0.2% at 662 keV. Of all the detectors compared, the CZT has the highest density of 6.0 g/cm^3, in contrast to 3.7 and 5.3 g/cm^3 for the NaI and $LaBr_3$ detectors respectively [45]. The higher density gives the CZT a slight advantage in photo-peak efficiency with more material for the ionizing radiation to interact with. The CZT detector is also reported to have no significant change in the energy spectrum when operating in temperatures from -10°C to 33°C [46].

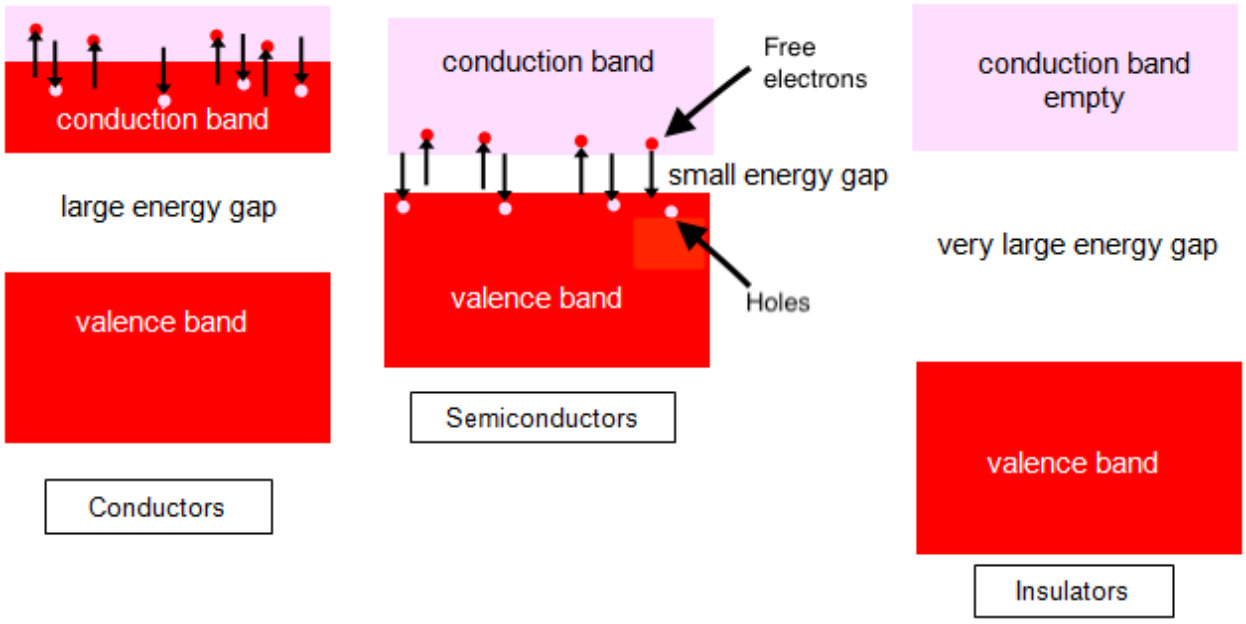


Fig. 4.4: Energy band structure for conductors, semiconductors and insulators.

The independence of temperature is an important parameter to consider since the ultimate goal of this project is to submerge this housing in a reactor pool which is reported to be >30°C [18]. The good resolution and the durability of this detector makes this a valuable detector for many fields.

Another beneficial property of the CZT detector is the ability to well calibrate the detector due to the very linear behavior of the calibration curve. Figures 4.5 & 4.6 show the calibration spectrum and calibration curve with sources of Co, Na, Mn, Ba, and Am. In the reactor pool, we have access to a Co, and a Cs source for calibration, this will be discussed in a later section. In the next section we will discuss other interested in the CZT gamma-ray detector.

4.5.1 Applications in Other Areas of Physics

Small volume (0.5 mm^3) CZT detectors have shown to be good detectors for underwater spent fuel element assays [47] because of their low detection efficiencies, due to small crystal sizes, and good resolution around the 662 keV peak. It was shown that small-sized CZT detectors can operate in high radiation fields with little effect on the detector itself. These detectors were sent underwater for gamma-ray spectrum measurements on spent fuel cores and accumulated 1000 counts per second (cps) for the small volume CZT (0.5 mm^3) and about 800,000 cps for the larger volume CZT detectors (500 mm^3). The small volume detector is reported to have an energy resolution of ∼1.6% at 662 keV, about half of the energy resolution of the CZT detector we are using at HFIR.

CZT detectors are also desirable in the medical radiation detection labs. GE discusses advancements in using CZT detectors rather than scintillator-based gamma camera as well as the advantages of CZT over their scintillator counterparts. CZT detectors have the advantage of less dead space around the detector, intrinsic spacial resolution, and direct conversion of incident radiation to current pulse signals. GE Healthcare discusses 3 types of medical detectors using CZT technology: a dynamic whole-body imaging system for small animals, a CZT-based cardiac camera, and molecular breast imaging, where spacial resolution and minimal dead space are key factors [48]. The CZT would improve nuclear medicine

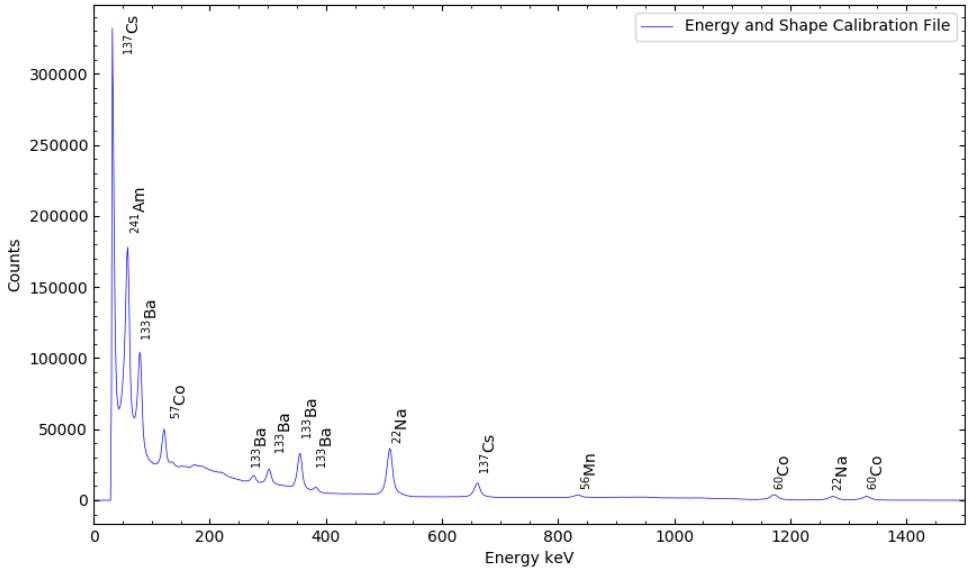


Fig. 4.5: Calibration spectrum of CZT detector using a variety of sources.

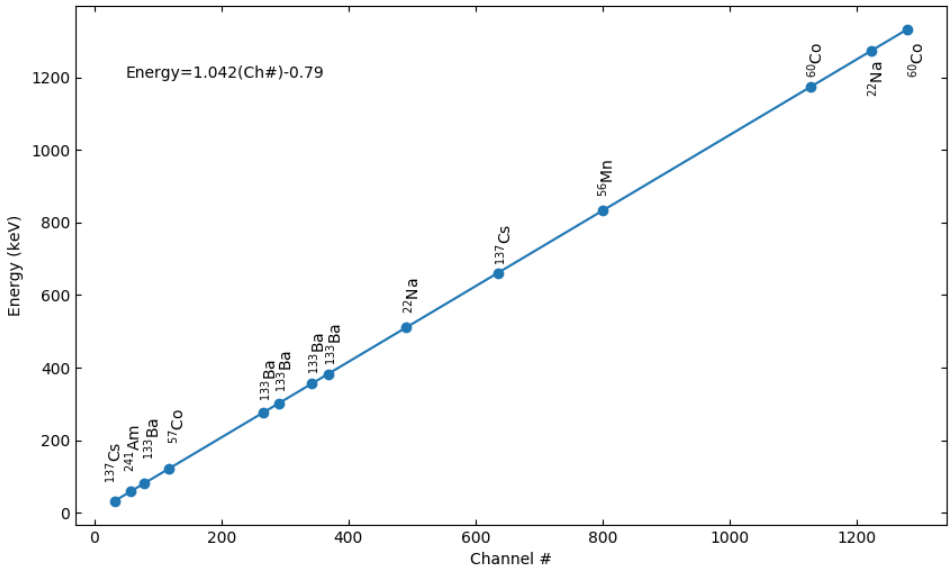


Fig. 4.6: Calibration curve of CZT detector using a variety of sources.

with its unique properties of size, and spacial and energy resolution. The next section will focus on the development of a system to protect the CZT detector from water-damage while it is submerged in a reactor pool.

4.6 Detector Housing Hardware Upgrade

To operate in a harsh environment such as HFIR, the detection housing must have quality control measures in place to ensure a smooth operation for the HFIR operators. The adaptation of a hygrometer inside of the housing has been an important addition to confirm that the seals of the housing have not been compromised. The hygrometer is sensitive enough to pick up small leaks of ∼5 mL, which otherwise would go un-noticed until effects are seen in the electronic signals. The system for monitoring the humidity inside of the detector housing operates similarly to the magnetometer system discussed in chapter 3. A Raspberry pi (3.3.1), I^2C signal extenders (3.3.5), and a hygrometer/temperature sensor board were used to develop a monitoring system using a Grafana server to display real-time data. This section will discuss the details of the humidity monitoring system design and setup.

4.6.1 Hygrometer Chip

A high accuracy hygrometer chip from Texas Instruments (model #: HDC1080) was used for the purpose of monitoring the humidity inside the detector housing. This chip features a relative humidity accuracy of ±2% and a temperature accuracy of ±0.2°C. It requires only 2.7 to 5.5 V, and 1.3μA for measurement, which does not exceed that given by a Raspberry Pi. The chip is available as a pre-soldered board, similar to the Adafruit magnetometers, section 3.3.3, where the pull up resistors necessary are all ready soldered and the board is ready to use. This board is soldered directly to a Sparkfun I2C Bus Extender to bring the signal through the 50 ft long cable out of the water. The signal travels through an Ethernet cable and is plugged in to the RPi (figure 4.7) where the data is collected, stored and plotted locally on a Grafana server (figure 4.8) within a Python program.

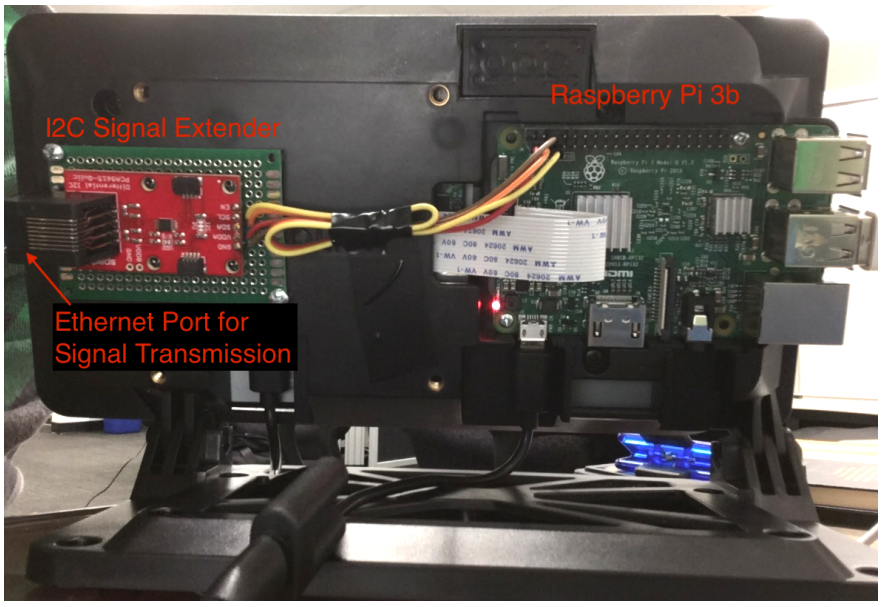


Fig. 4.7: View of the back of the RPi 7 inch touchscreen to show mounting of I2C signal extender and RPi.



Fig. 4.8: Locally hosted Grafana server to display the environmental conditions inside the housing.

4.6.2 Data Collection

The data requested from the sensor board by the Python program is collected and stored in the RPi for analysis and graphing. The program reads the temperature and humidity from the sensor every 500μs and calculates the rate of change of the humidity over the past 10 data points (5 seconds). This rate of change value is used to determine if the humidity is increasing more than what is considered safe. This threshold will be defined in a later section. All the data is stored locally on the RPi in a time-stamped text file as well as in a time-series database, InfluxDB.

4.6.3 InfluxDB

InfluxDB is a time-series database for fast logging of large amounts of time-stamped data, such as environmental metrics as a function of time, or other time-stamped events. To write to InfluxDB, a program collects all the data it needs and stores it as a variable. These variables are then sent to the InfluxDB Docker container (section: 4.6.4) in a Hypertext Transfer Protocol (HTTP) message body. Once the data is stored in InfluxDB, it can be accessed by looking at the assigned InfluxDB address. More detailed information about how InfluxDB works can be found at the InfluxDB website [49].

4.6.4 Docker

Docker is a software suite where an isolated software package, "container", can be opened for a specific program (ie. InfluxDB or Grafana), and can communicate through defined channels, also known as ports. In this setup, the InfluxDB Docker container is assigned to one local port (ie. 0.0.0.0:8017), and the Grafana Docker container is assigned to another (ie. 0.0.0.0:3000). In this configuration, Grafana (section: 4.6.5) can be programmed to look at port 0.0.0.0:8017 every second for new data. More detailed information about how Docker works can be found at the Docker website [50].

4.6.5 Grafana Server

Grafana is an open platform for elegant analytics and monitoring. This powerful tool helps to bring several different types of databases to one place for visual representation. Grafana unifies 30+ databases in a variety of applications, such as: server statistics (ie. server traffic, connected devices, etc.), computer parameters (ie. CPU load & temperature, storage space availability, etc.), and environmental parameters (ie. temperature and humidity of different zones, local weather, local magnetic fields, etc.). In this thesis, we use Grafana for reliable monitoring of environmental metrics.

Grafana servers are accessed via a web-browser by a local user connecting to the specific web-address (ie. http://0.0.0.0:3000). If configured, this server page can be hosted and accessed by anyone with an internet connection outside of the local network.

4.6.6 Humidity Monitoring Setup and Configuration

The leak detection system was built to be simple, yet reliable for detecting small amounts of water entering the detector housing. The data collected from the hygrometer and thermometer board is stored in a text file as well as in an InfluxDB database. This database and Grafana program are hosted in their own Docker container allowing them to communicate to each other through define ports in the local network. The Grafana visualization server is accessed via web-browser, which is hosted locally on the RPi. Since ORNL maintains a tight internet security, this server is exclusively hosted on the local RPi and does not broadcast any data, or open any ports in the internal network. With a reliable server that can operate for days without interruption, and a sensitive instrument for leak detection, we are able to focus on the measurements on the fuel core with assurance that the detectors will not be compromised. In the next section, we introduce the determination of the sensitivity of the hygrometer board.

4.7 Hygrometer Results

4.7.1 Testing Setup

To test the response of the hygrometer, a 5 gallon bucket with an o-ring sealed lid was used as the testing container where a small leak would be simulated. Three holes were drilled into the lid to allow the Ethernet communication line, nitrogen drying line, and the water dropper into the bucket. This setup is shown in figure 4.9 & 4.10.

Several different tests were conducted on the bucket in an attempt to best simulate the real environment of a reactor pool. According to the HFIR User Guide [17], coolant temperatures can reach upwards of 50°C. The bucket tests were conducted at both room temperature (21-23°C) and a high temperature approaching, as best as possible, 30°C. Humidity was initially controlled by drying out the bucket with nitrogen and then turned off for the simulated leak. The purpose of the bucket tests were to characterize and understand the behavior of a sealed environment when unwanted moisture enters.

4.7.2 Sealed Bucket Tests

Four different tests were conducted with the sealed bucket to test the sensitivity of the hygrometer and determine a threshold in the rate of change of the humidity for a detected leak. The detector housing and this bucket are not hermetically sealed, therefore it should be expected that given enough time, the housing will equalize its humidity with that of the room. For this reason, we monitor the rate of change of the humidity rather than the relative humidity of either container.

The initial temperature and initial humidity were varied to test the sensitivity under different environmental conditions. Table 4.2 lists the starting temperature and humidity conditions as well as the average and maximum rate of change for 1 minute after injecting $\sim$3 ml of water into the bucket. It can be seen that with a higher initial temperature, overall higher rate of change in the humidity is observed. To be conservative, we defined the leak threshold to be the lowest average rate of change observed during these tests. A leak is now defined as a rate of change of at least 2 % per minute.

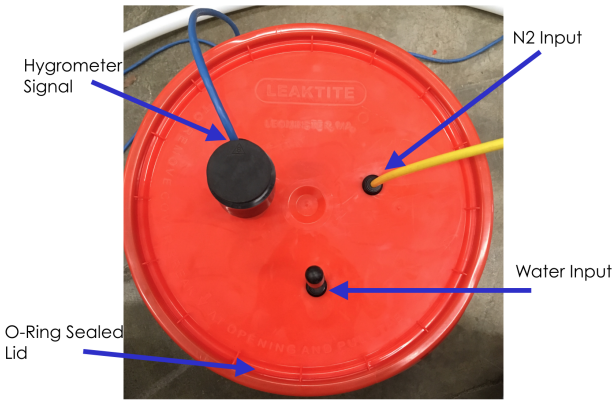


Fig. 4.9: Setup of 5 gallon o-ring sealed Leaktite bucket.



Fig. 4.10: View of the testing bucket with attached electronics.

Table 4.2: Average rate of change of the humidity for 1 minute after leak is injected into the sealed bucket. The initial conditions for temperature and humidity are given.

Temp. (C)	Humidity (%)	Avg. Rate of Change (% per min.)	Max Rate of Change (% per min.)
30	41	7.37	9.6
28	4.1	5.97	9.1
23	48	2.34	4.4
21	3.9	3.8	6.1

4.7.3 Results Inside Empty Detector Housing

The detector housing was initially tested for water-tightness with the housing empty. It was first dried with nitrogen and the hygrometer was placed inside to monitor the humidity. Figure 4.11 shows the housing being lowered into the water for testing. On one occasion, the housing leaked within a few seconds of being submerged. The leak can be seen in figure 4.12. The humidity started increasing at a rate well above the 2%/minute threshold that was defined as the trigger point for leaks. Upon inspection of the housing, about 10 mL of water leaked in due to a faulty o-ring seal. Over a weekend, the housing was submerged to test its ability to withstand water pressure over a prolonged period of time. This test is shown in figure 4.13. The humidity is always increasing as expected due to the small amount of exchange through the cable port, this is the cause of the rate of change fluctuations observed. The rate of change of humidity never exceeds 1%/minute during this time. The housing showed no signs of leaking when it was opened for inspection. With successful submersion tests complete, the housing was sent to the HFIR reactor pool.

4.8 Gamma Scanning in Reactor Pool

The detector housing has been fully operational with several days worth of underwater data taking. No leaks have been detected, and the electronics have shown no signs of failing. The CZT detector has been performing well and initial results from the reactor bay gave us the information we needed to optimize the system of measurement. Initial results from the reactor pool showed a large build-up of Compton down scattered gamma-rays due to the amount of water between the source and the detector. To reduce Compton down scattered spectra and improve the quality of the spectra, a double collimator was used in a 4 ft. air filled tube before the detector. This allowed us to get good peak-to-total ratios, good position resolution, and a reduced count rate. The data is currently being analyzed internally using a variety of software. Radware is being used to fit peaks and study the the response of the detector at various energies. Python is also being used for a quick spectrum to spectrum comparison and plotting. Every day the first spectrum measured is an energy calibration on 2 different sources. Figure 4.14 shows an underwater gamma spectrum using a ^{60}Co and

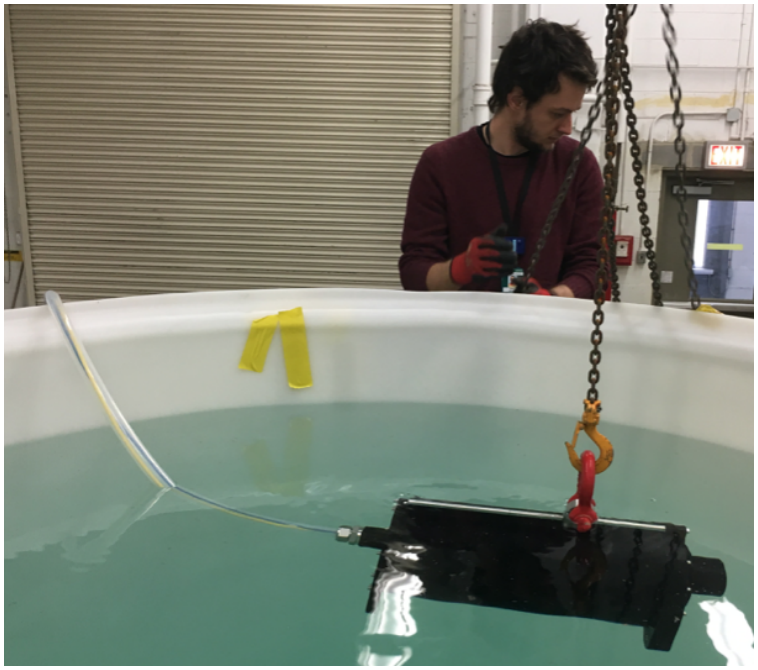


Fig. 4.11: Lowering of submarine into the testing bucket while watching the leak detection system server for alerts.

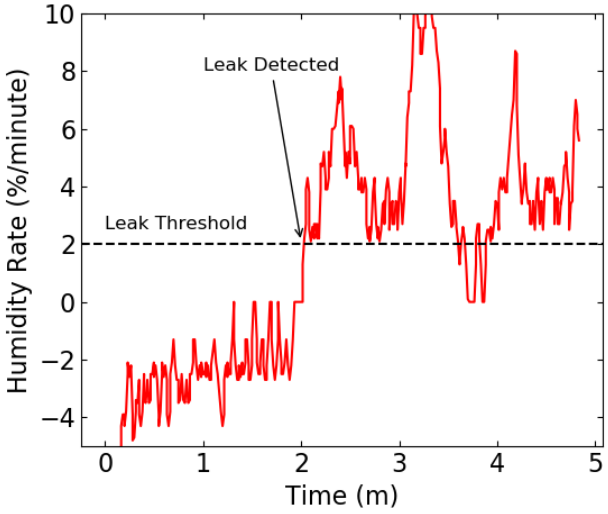


Fig. 4.12: housing being submerged with a faulty o-ring seal.

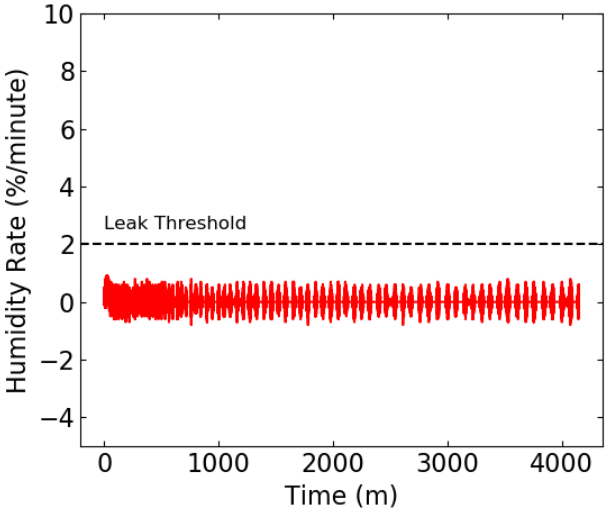


Fig. 4.13: Submerged housing over 60 hours with no sign of leak.

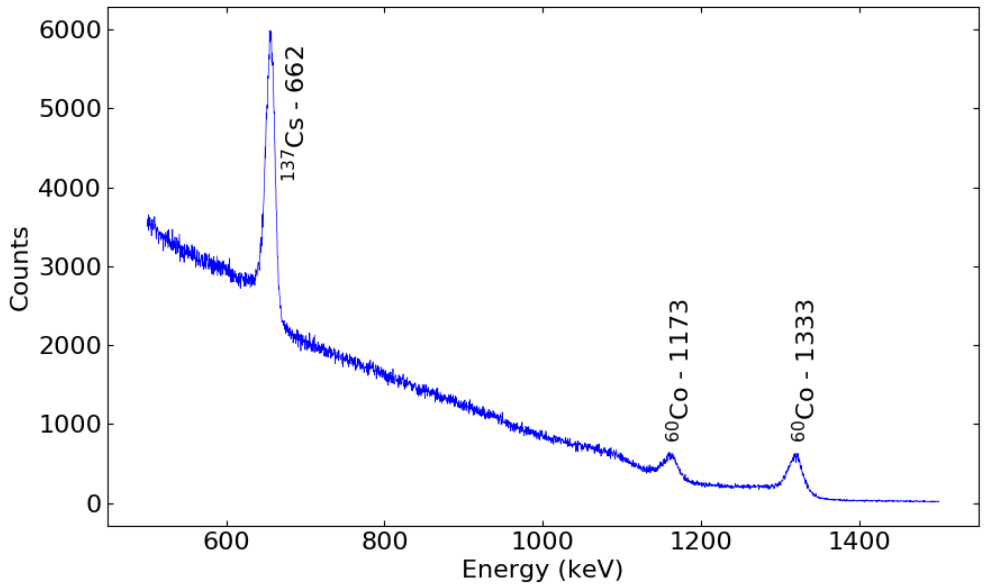


Fig. 4.14: Underwater Source check with 4ft. tube and double collimation setup. Fitting is done in Radware where we extract peak parameters (ie. width) and check energy calibration.

a ^{137}Cs calibration sources. The fitting of the calibration peaks was done using Radware and the parameters are extracted. In this figure, the peaks correspond to a ^{137}Cs and two ^{60}Co peaks with widths of 34.1, 51.4 and 60.3 keV respectively. These parameters can than be fixed in Radware in an attempt to discriminate multiple peaks that are too close for the CZT detector to resolve when analyzing the spectrum from the fuels.

4.9 Conclusion

A leak detection system has allowed the safe operation of a CZT gamma-ray detector underwater in the HFIR reactor pool. The pool is a difficult operation environment for the gamma-ray detector due to the high radiation and high temperatures. This harsh environment demands a simple robust system that can withstand a high number of counts and operate uniformly in a variety of temperatures. Because of the lower efficiency of the

CZT detector, it has performed well in the radiation field environment with heavy collimation to reduce Compton down scatter as well as the count rate. The CZT has shown no signs of degradation since initial operation. Results for this project will be published in an internal report.

Chapter 5

Conclusions and Future Work

5.1 Summary of Results

Two compact and robust systems for real-time monitoring of environmental conditions have been developed, programmed and fully implemented into their respective experiments. Each system is powered by a Raspberry Pi and collects data with various sensors via I^2C signal cable for data analysis, and real-time graphical representation. These systems were designed to be easy to setup and adapt to a specific experiment at a low cost. With the ability to communicate with up to 1008 sensors, this system can monitor a wide range of parameters without the need for multiple systems. A couple examples of parameters that can be measured are: capacitive soil moisture sensor, light sensors, lightning sensor, current sensors, and CO, alcohol and volatile organic compounds (VOC) sensors.

The data from the system of magnetometers around PROSPECT has been fully integrated into the slow control server is actively monitoring for spikes in the magnetic background. If a high magnetic field is observed, the data analysis team can discriminate that data and inspect it for any possible PMT gain and pulse shape distortion. This system has been working continuously since its installation in October 2018 and has shown to be effective in detection of the operation of an 8 T magnet on beamline 2 in HFIR. The magnetometers will continue to operate throughout the lifetime of PROSPECT.

The hygrometer system for the detector housing has also been operating continuously to monitor the conditions inside of the watertight detector housing. This has been a critical

system to ensure the safety of the gamma-ray detection equipment inside of the housing. This monitoring system was able to communicate to the HFIR operation team that the detector housing has not been compromised and it was safe to continue with the experiment while submerged in the reactor pool.

5.2 Future Work

Implementing an assay system for reactor fuel cores before the introduction of neutrons could be a very practical and useful system to avoid damages and potential contamination in HFIR. The gamma-ray detector housing has been proven to be able to function underwater in a harsh environment and more advanced technologies could be investigated.

Bibliography

[1] F. P. An *et al.*, "Measurement of the reactor antineutrino flux and spectrum at daya bay," *Phys. Rev. Lett.*, vol. 116, p. 061801, Feb 2016. xi, 5, 6

[2] J. Ashenfelter *et al.*, "The PROSPECT physics program," *Journal of Physics G: Nuclear and Particle Physics*, vol. 43, p. 113001, oct 2016. xi, 11, 13, 14

[3] J. Navarro, R. Aryaeinejad, and D. Nigg, "A feasibility study to determine cooling time and burnup of advanced test reactor fuel using a nondestructive technique and three types of gamma-ray detectors," *Journal of ASTM International*, vol. 9, pp. 1–16, 2012. xii, 33, 34

[4] L. M. Brown, "The idea of the neutrino," *Physics Today*, vol. 31, no. 9, pp. 23–28, 1978. 4

[5] F. Reines and C. L. Cowan, "Neutrino physics," *Physics Today*, vol. 10, no. 8, pp. 12–18, 1957. 4

[6] G. Zacek *et al.*, "Neutrino-oscillation experiments at the gösgen nuclear power reactor," *Phys. Rev. D*, vol. 34, pp. 2621–2636, Nov 1986. 4

[7] A. I. Derbin *et al.*, "Experiment on anti-neutrino scattering by electrons at a reactor of the Rovno nuclear power plant," *JETP Lett.*, vol. 57, pp. 768–772, 1993. [Pisma Zh. Eksp. Teor. Fiz.57,755(1993)]. 4

[8] V. P. Martemyanov *et al.*, "The kr2det project: Search for mass-3 state contribution —ue3—2 to the electron neutrino using a one-reactor-two-detector oscillation experiment at the krasnoyarsk underground site," *Physics of Atomic Nuclei*, vol. 66, pp. 1934–1939, Oct 2003. 4

[9] Z. D. Greenwood *et al.*, "Results of a two-position reactor neutrino-oscillation experiment," *Phys. Rev. D*, vol. 53, pp. 6054–6064, Jun 1996. 4

[10] Y. Declais *et al.*, "Search for neutrino oscillations at 15-meters, 40-meters, and 95-meters from a nuclear power reactor at Bugey," *Nucl. Phys.*, vol. B434, pp. 503–534, 1995. 4

[11] G. Mention *et al.*, "Reactor antineutrino anomaly," *Phys. Rev. D*, vol. 83, p. 073006, Apr 2011. 4

[12] J. K. Ahn *et al.*, "Observation of reactor electron antineutrinos disappearance in the reno experiment," *Phys. Rev. Lett.*, vol. 108, p. 191802, May 2012. 5

[13] Y. Abe *et al.*, "Indication of reactor $\overline{\nu}_e$ disappearance in the double chooz experiment," *Phys. Rev. Lett.*, vol. 108, p. 131801, Mar 2012. 5

[14] P. Huber, "Determination of antineutrino spectra from nuclear reactors," *Phys. Rev. C*, vol. 84, p. 024617, Aug 2011. 5

[15] T. A. Mueller *et al.*, "Improved predictions of reactor antineutrino spectra," *Phys. Rev. C*, vol. 83, p. 054615, May 2011. 5

[16] J. Kopp *et al.*, "Sterile neutrino oscillations: the global picture," *Journal of High Energy Physics*, vol. 2013, p. 50, May 2013. 5

[17] "High flux isotope reactor user guide." https://neutrons.ornl.gov/sites/default/files/High Accessed: May 15, 2019. 5, 45

[18] "High flux isotope reactor." https://neutrons.ornl.gov/hfir. Accessed: May 15, 2019. 5, 33, 39

[19] A. N. Laboratory. https://www.rertr.anl.gov/, 2019. 8

[20] D. C. G. Ilas *et al.*, "Modeling and simulations of the high flux isotope reactor cycle 400," *Tech. Rep. ORNL/TM-2015/36*, 2015. 8

[21] J. Ashenfelter *et al.*, "A low mass optical grid for the PROSPECT reactor antineutrino detector." arXiv:1902.06430, 2019. 11

[22] J. Ashenfelter *et al.*, "The PROSPECT reactor antineutrino experiment." arXiv:1808.00097, 2018. 11

[23] J. Ashenfelter *et al.*, "Lithium-loaded liquid scintillator production for the PROSPECT experiment," *Journal of Instrumentation*, vol. 14, pp. P03026–P03026, mar 2019. 11

[24] B. A. Heffrom, *Characterization of Reactor Background Radiation at HFIR for the PROSPECT Experiment*. MS thesis, University of Tennessee, 2017. 11

[25] E. Technology. https://eljentechnology.com/products/liquid-scintillators/ej-301-ej-309, 2019. 11

[26] C. E. Aalseth *et al.*, "Search for neutrinoless double-β decay in ^{76}Ge with the majorana demonstrator," *Phys. Rev. Lett.*, vol. 120, p. 132502, Mar 2018. 11, 13

[27] K.-H. Ackermann *et al.*, "The gerda experiment for the search of $0\nu\beta\beta$ decay in 76ge," *The European Physical Journal C*, vol. 73, p. 2330, Mar 2013. 11

[28] Nuclear Science Advisory Committee, "Neutrinoless double beta decay," 2015. 13

[29] C. C. and, "Background model for the majorana demonstrator," *Journal of Physics: Conference Series*, vol. 888, p. 012240, sep 2017. 13

[30] J. Ashenfelter *et al.*, "First search for short-baseline neutrino oscillations at hfir with prospect," *Phys. Rev. Lett.*, vol. 121, p. 251802, Dec 2018. 13

[31] "Neutron scattering and high magnetic fields workshop report." https://neutrons.ornl.gov/content/neutron-scattering-and-high-magnetic-fields-workshop-report. Accessed: May 15, 2019. 15

[32] J. Boyle, *Characterizing the Effects of Ambient Magnetic Fields on Photomultiplier Tubes and Monitoring Muon Flux for PROSPECT*. MS thesis, University of Tennessee, 2018. 16, 17, 18

[33] N. Allemandou *et al.*, "The stereo experiment," *Journal of Instrumentation*, vol. 13, 04 2018. 16

[34] P.-L. Wang, Y.-L. Zhang, X.-L. Wang, and Z.-Z. Xu, "Magnetic shielding for DAMPE electromagnetic calorimeter PMTs," *Chinese Physics C*, vol. 38, p. 086002, aug 2014. 16

[35] R. M. Faradzhaev, Y. A. Trofimov, E. E. Lupar, and V. N. Yurov, "Performances investigation and material selection of PMT magnetic shields for the space experiments with GRIS and PING-m instruments," *Journal of Physics: Conference Series*, vol. 675, p. 042008, feb 2016. 16

[36] E. Jeon, J. Kim, Y. Kim, K. Ma, and J. Nam, "Magnetic field effects on the photocathode uniformity of hamamatsu r7081 photomultiplier tubes," *Nuclear Instruments and Methods in Physics Research Section A: Accelerators, Spectrometers, Detectors and Associated Equipment*, vol. 697, pp. 46 – 51, 2013. 16

[37] Hamamatsu Photonics K.K., *Photomultiplier Tubes Basics and Applications*. Hamamatsu City: Hamamatsu Photonics K.K., 2007. 17, 18

[38] "Nanocrystalline soft magnetic material." https://www.hitachi-metals.co.jp/products/elec/tel/pdf/hl-fm9-h.pdf. Accessed: May 15, 2019. 20

[39] "Ultra-compact high-performance ecompass module: 3d accelerometer and 3d magnetometer datasheet." https://www.mouser.com/datasheet/2/389/lsm303dlhc-955106.pdf. Accessed: May 15, 2019. 21

[40] C. Gilbert, "Server code." https://github.com/coreyeg3/Server-Code, 2018. 23, 24

[41] NOAA, "Magnetic declination estimated value." https://www.ngdc.noaa.gov/geomag/calculators/magcalc.shtml?, 2019. 24

[42] AIP FYI Bulletin, "DOE and NIST considering long-term research reactor plans." 33

[43] W. Leo, *Techniques for Nuclear and Particle Physics Experiments: A How-to Approach*. Springer, 1994. 37

[44] eV Products. http://www.umich.edu/~ners580/ners-bioe_481/lectures/pdfs/SemiConductor-material_prop.pdf,, 2013. 38

[45] D. T. Vo, "Comparison of portable detectors for uranium enrichment measurements," *International Topical Conference Methods and Applications of Radioanalytical Chemistry VII (MARC VII)*, 2006. 38

[46] S.-D. Chun *et al.*, "Property of a czt semiconductor detector for radionuclide identification," *Journal of Nuclear Science and Technology*, vol. 45, no. sup5, pp. 421–424, 2008. 38

[47] V. Ivanov *et al.*, "Miniature cdznte detectors for application in high intensity radiation fields," pp. 398 – 402, 11 2008. 39

[48] G. Healthcare, "White paper: Czt technology: Fundamentals and applications," Tech. Rep. MWS DOC0701734, General Electric Company, Waukesha, WI, 2009. 39

[49] InfluxDB. https://www.influxdata.com/, 2019. 43

[50] Docker. https://www.docker.com, 2019. 43

Vita

Corey E. Gilbert Graduated from Stockton University in 2016 with a Bachelors of Science in Applied Physics. Starting in 2016, Corey continued his physics education at the University of Tennessee in Knoxville and is expected to graduate in August of 2019 with a MS. in Physics. Corey plans to continue working in a physics environment to help the experimental community with problem solving.